A Letter of Intent on Nuclear and Particle Physics Experiments at the J-PARC 50 GeV Proton Synchrotron

An Experimental Search for $\mu^- - e^-$ Conversion at a Sensitivity of 10^{-16} with a Slow-Extracted Bunched Beam

December 15th, 2006

.

Abstract

We request support to develop a proposal for a new experiment of searching for coherent neutrino-less conversion of muons to electron ($\mu^- - e^-$ conversion), $\mu^- + N(A,Z) \rightarrow e^- + N(A,Z)$, in muonic atoms at a sensitivity of $B(\mu^- N \rightarrow e^- N) < 10^{-16}$. The aimed sensitivity is a factor of 10,000 better than that of current experiments. This experiment would offer powerful probe for new physics phenomena beyond the Standard Model. The experiment is planned to be carried out in the J-PARC Nuclear and Particle Experimental (NP) Hall by using a bunched proton beam slowly extracted from the J-PARC main ring, where beam bunching is needed to eliminate beam-related backgrounds. The muon beamline considered consists of high-field pion capture solenoids, curved solenoids to select beam momenta, and a curved solenoid spectrometer to detect $\mu^- - e^-$ conversion with low-counting-rate conditions. In our previous Letter of Intent, an experiment aiming for 10^{-18} sensitivity (PRISM) with a muon storage ring and a fast extracted proton beam was presented. This new initiative has been taken recently to achieve an early and timely start of a series of searches and is regarded as the first step of our staging approach continuing toward the ultimate search and the discovery of $\mu^- - e^-$ conversion.

Contents

Chapter 1

Physics Motivation

1.1 Introduction

Recently, lepton flavor violation of charged leptons (LFV)[1] has attracted much interest from theorists and experimentalists in particle physics, since it has a growing potential to find an important clue of new physics beyond the Standard Model [1]. Some of the notable features on the LFV studies are that (1) LFV might have sizable contributions from new physics considered, which could be observable in future experiments, and (2) LFV does not have any sizable Standard Model contribution (such as from neutrino mixing), which could become serious background otherwise.

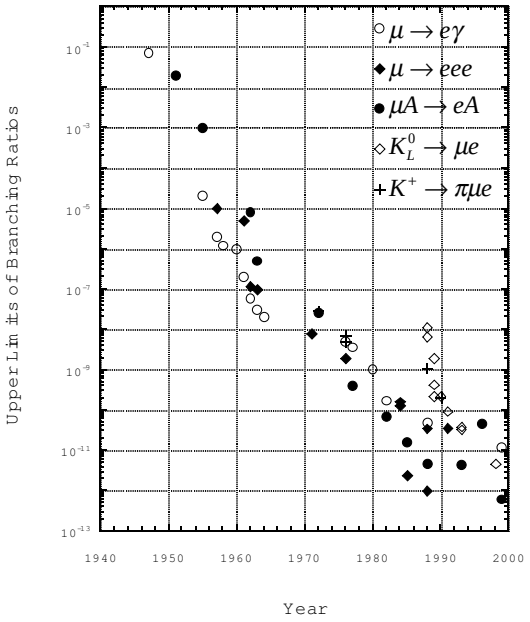

Figure 1.1: History of searches for LFV in muon and kaon decays

[1]It is also called charged-lepton mixing.

Historically, the search for LFV has been initiated by Hincks and Pontecorvo in 1947 [2]. Since then, the searches for LFV have been continuously carried out with various elementary particles, like muons, kaons and others. The upper limits have been improved at a rate of two orders of magnitude per decade, as seen in Fig. 1.1.

The muon system is one of the best places to search for LFV [1]. The upper limits of various LFV decays are listed In Table 1.1, where it is seen that the sensitivity to LFV is superb in the muon system. It is mostly because of a large number of muons available for experimental searches today (of about $10^{14} - 10^{15}$ muons/year). And more muons (of about $10^{18} - 10^{19}$ muons/year) would be available in future if a new highly intense muon source is realized.

Table 1.1: Limits of the lepton-flavor violating decays of muon, tau, pion, kaon and Z boson.

Reaction	Present limit	Reference
$\mu^+ \to e^+\gamma$	$< 1.2 \times 10^{-11}$	[3]
$\mu^+ \to e^+e^+e^-$	$< 1.0 \times 10^{-12}$	[4]
$\mu^- Ti \to e^- Ti$	$< 6.1 \times 10^{-13}$	[5]
$\mu^+e^- \to \mu^-e^+$	$< 8.3 \times 10^{-11}$	[6]
$\tau \to e\gamma$	$< 3.9 \times 10^{-7}$	[7]
$\tau \to \mu\gamma$	$< 3.1 \times 10^{-7}$	[8]
$\tau \to \mu\mu\mu$	$< 1.9 \times 10^{-7}$	[9]
$\tau \to eee$	$< 2.0 \times 10^{-7}$	[9]
$\pi^0 \to \mu e$	$< 8.6 \times 10^{-9}$	[10]
$K_L^0 \to \mu e$	$< 4.7 \times 10^{-12}$	[11]
$K^+ \to \pi^+\mu^+e^-$	$< 2.1 \times 10^{-10}$	[12]
$K_L^0 \to \pi^0\mu^+e^-$	$< 3.1 \times 10^{-9}$	[13]
$Z^0 \to \mu e$	$< 1.7 \times 10^{-6}$	[14]
$Z^0 \to \tau e$	$< 9.8 \times 10^{-6}$	[14]
$Z^0 \to \tau\mu$	$< 1.2 \times 10^{-5}$	[15]

In the minimal Standard Model, lepton flavor conservation is built in by hand with assuming vanishing neutrino masses. However, neutrino mixing has been experimentally confirmed by the discovery of neutrino oscillation. Now, lepton flavor conservation is known to be violated. However, LFV has yet been observed experimentally. It is known that the contribution of neutrino mixing to LFV is extremely small, since it is proportional to $(m_\nu/m_W)^4$, yielding the order of 10^{-50} in branching ratios. Therefore, discovery of LFV would imply new physics beyond "neutrino oscillation". As a matter of fact, any new physics or interaction beyond the Standard Model would predict LFV at some level.

The physics motivation of LFV is very robust for next decade. To illustrate, let us consider two possible physics cases, depending on whether LHC find supersymmetry (SUSY).

1.2 Supersymmetric Extension

It is known that LFV has significant contributions from SUSY, if SUSY particles exist in the LHC energy range. In this case, studies of LFV would focus on SUSY. In SUSY models, the SUSY contributions can be presented by the slepton mass matrix ($m_{\tilde{l}}^2$), given in Eq. (1.1).

$$m_{\tilde{l}}^2 = \begin{pmatrix} m_{\tilde{e}\tilde{e}}^2, \Delta m_{\tilde{e}\tilde{\mu}}^2, \Delta m_{\tilde{e}\tilde{\tau}}^2 \\ \Delta m_{\tilde{\mu}\tilde{e}}^2, \ m_{\tilde{\mu}\tilde{\mu}}^2, \Delta m_{\tilde{\mu}\tilde{\tau}}^2 \\ \Delta m_{\tilde{\tau}\tilde{e}}^2, \Delta m_{\tilde{\tau}\tilde{\mu}}^2, \ m_{\tilde{\tau}\tilde{\tau}}^2 \end{pmatrix} \tag{1.1}$$

The SUSY contributions to LFV depend on an off-diagonal element $\Delta m_{\tilde{\mu}\tilde{e}}^2$ or $\Delta m_{\tilde{e}\tilde{\mu}}^2$.[2] Therefore, the determination of these SUSY contributions would enable us to study the slepton mass matrix and therefore SUSY (soft) breaking. In the following, the SUSY contributions to LFV is presented in more details.

In minimum SUSY models, charged lepton mixing would occur through mixing of their corresponding sleptons. Fig.1.2 shows one of the SUSY diagrams contributing to muon to electron transition, where the mixing of smuon ($\tilde{\mu}$) and selectron ($\tilde{e}$) is given by an off-diagonal slepton mass matrix $\Delta m_{\tilde{\mu}\tilde{e}}^2$. In minimum SUSY models, the slepton mass matrix is assumed to be a diagonal matrix at the Planck mass scale (10^{19} GeV), and no off-diagonal matrix elements exits ($\Delta m_{\tilde{\mu}\tilde{e}}^2 = 0$). Then, non-zero off-diagonal matrix elements can be induced by radiative corrections from the Planck scale to the weak scale ($\sim 10^2$ GeV). There could be two scenarios at high energy to induce off-diagonal elements of the slepton mass matrix. One is grand unification (GUT) where the GUT Yukawa interaction creates non-zero off-diagonal elements. This scenario is called **SUSY-GUT** models. And the other is Seesaw mechanism, where the neutrino Yukawa interaction does. This is called **SUSY-Seesaw** models. Both of the models predict the branching ratios of LFV from just below to a few orders of magnitude below the current experimental upper limits. Therefore, if we

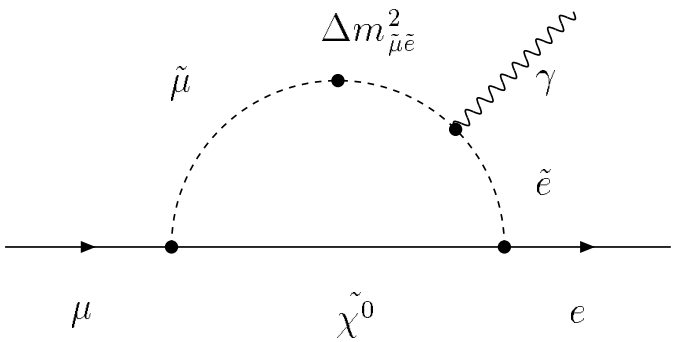

Figure 1.2: One of the diagrams of SUSY contributions to a μ to e transition. $\Delta m_{\tilde{\mu}\tilde{e}}^2$ indicates the magnitude of the slepton mixing.

[2]Similarly, the SUSY contributions to the muon $g-2$ and the muon EDM are a real and an imaginary parts of the diagonal element $m_{\tilde{\mu}\tilde{\mu}}^2$, respectively.

could improve experimental sensitivity by a few orders of magnitude, this would provide great discovery potential.

1.2.1 Prediction of SUSY-GUT Models

In SUSY-GUT, the non-zero slepton mixing appears unavoidably through radiative corrections in the renormalization group evolution from the GUT scale to the weak energy scale [16]. It is given by

$$\Delta m^2_{\tilde{\mu}\tilde{e}} \propto \frac{3m_0^2 + A_0^2}{8\pi^2} h_t^2 V_{td}^* V_{ts} \ln \frac{M_{GUT}}{M_{R_3}} \tag{1.2}$$

where m_0 is the universal scalar mass. V_{td} and V_{ts} are the Kobayashi-Maskawa (KM) quark mixing matrix elements. Recently, it was pointed out that the slepton mixing thus generated is very large owing to the large top-quark Yukawa coupling [17]. The branching ratios of $\mu^- - e^-$ conversion predicted in SUSY SU(5) models [1] are shown in Fig. 1.3. They range from 10^{-15} to 10^{-13} for the singlet smuon mass of $m_{\tilde{\mu}_R}$ of 100 to 300 GeV [18]. They are larger for a large $\tan\beta$ value. The SO(10) SUSY GUT models give an even larger value of 10^{-13} to 10^{-11} by an enhancement of $(m_\tau^2/m_\mu^2) \sim 100$ [17]. It is because of the existence of loop diagrams whose magnitude is proportional to the tau-lepton mass in SO(10) SUSY-GUT models.

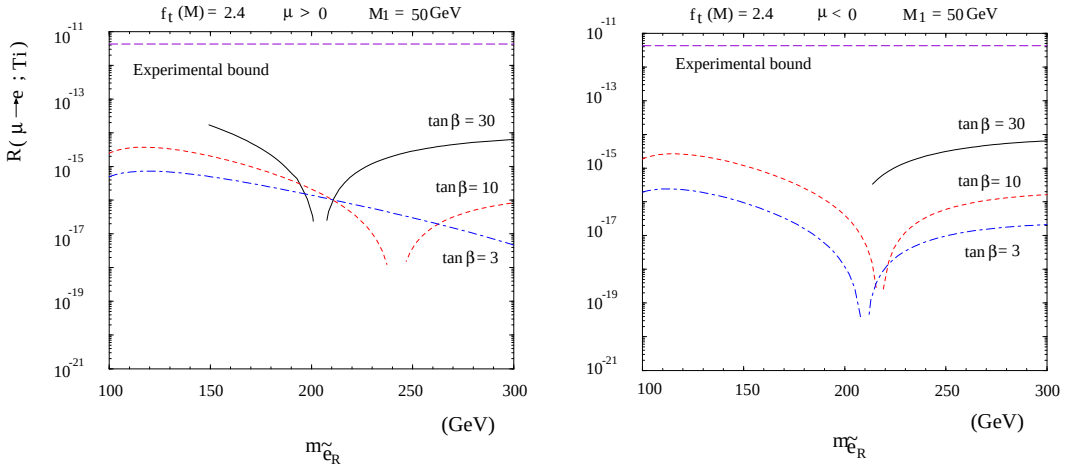

Figure 1.3: Predicted branching ratios for $\mu^- - e^-$ conversion in SUSY-GUT. μ is one of the SUSY parameters, and $\mu > 0$ (left) and $\mu < 0$ (right).

1.2.2 Predictions of SUSY-Seesaw Models

The other model is supersymmetric models with the seesaw mechanism, which predict the existence of right-handed heavy neutrinos. As widely known, there is experimental evidence for the existence of neutrino masses and their mixing. In the SUSY model with the seesaw mechanism, the slepton mixing can be induced from the neutrino

mixing. Then, LFV processes in muon decays are also expected to occur [19, 20, 21]. In principle, there can be potentially two contributions to the slepton mixing $\Delta m^2_{\tilde{\mu}\tilde{e}}$. One is from $U_{\mu e}$ corresponding to the solar neutrino mixing. The other is from the product of $U_{\tau e}$ and $U_{\tau\mu}$ that corresponds to the atmospheric neutrino mixing. Assuming the tau Yukawa coupling is large, the second contribution can be large. In this case, the slepton mixing can be given by

$$\Delta m^2_{\tilde{\mu}\tilde{e}} \propto \frac{3m_0^2 + A_0^2}{8\pi^2} h_\tau^2 U^*_{\tau e} U_{\tau\mu} \ln \frac{M_{GUT}}{M_{R_3}} \tag{1.3}$$

where $U_{\tau e}$ and $U_{\tau\mu}$ are the Maki-Nakagawa-Sakata (MNS) neutrino mixing matrix elements. h_τ is the tau Yukawa coupling. The prediction is shown in Fig.1.4.

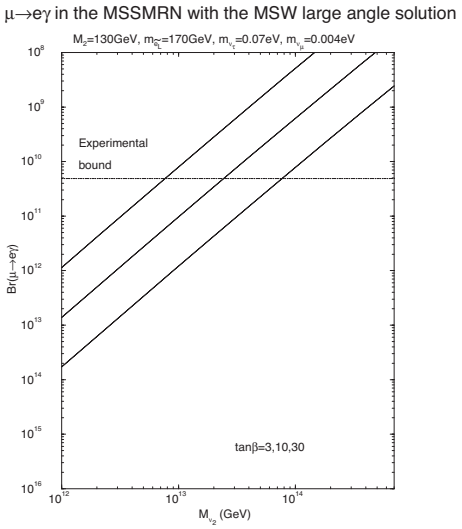

Figure 1.4: Predictions of $\mu^+ \to e^+\gamma$ branching ratio in SUSY-Seesaw models. The three lines correspond to the cases of $\tan\beta = 30, 10, 3$ respectively.

Fig.1.5 shows the two possible mechanisms to make slepton mixing in MSSM (supergravity SUSY). In SUSY-GUT cases, the slepton mixing is given by the product of the KM matrix elements, while in SUSY-Seesaw cases, it is given by the product of the MNS matrix elements. When LHC finds SUSY, charged lepton mixing attract more interest, in terms of studying either SUSY-GUT or SUSY-Seesaw models, rather than just minimum SUSY itself.

When LHC does not find SUSY, two cases can be considered; either no SUSY at all or heavier SUSY at multi TeV scale. High precision frontier with intense slow muons comes to the forefront, since it is sensitive to heavier mass scale than that high-energy accelerators can reach. For LFV, besides SUSY, there are other models to predict LFV, such as heavy neutrino models, leptoquark models, composite, two Higgs doublet models, second Z' models, anomalous Z coupling, and so on.

For heavier SUSY, if the LFV search has sufficient experimental sensitivity (such as 10^{-18} for $\mu^- - e^-$ conversion), it is sensitive to the SUSY mass scale up to several

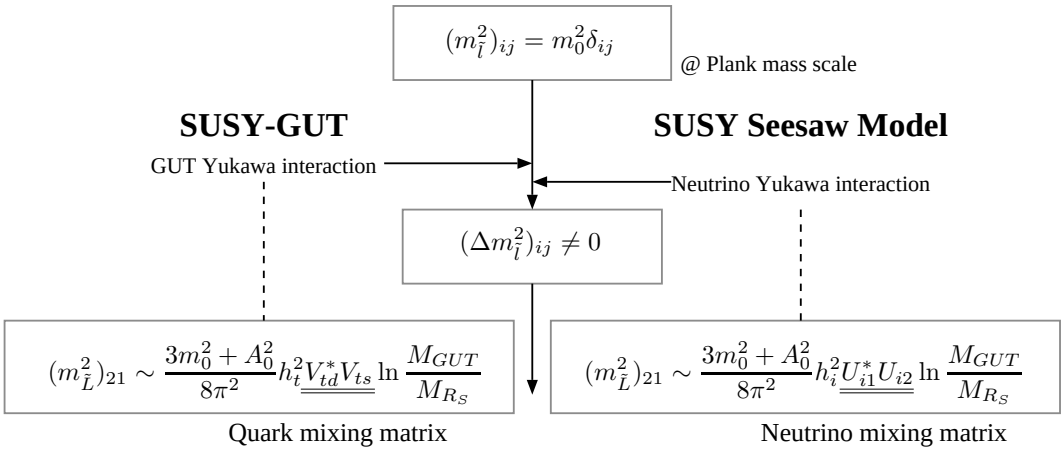

Figure 1.5: Two physics mechanisms (SUSY-GUT and SUSY-Seesaw) to introduce the slepton mixing in the MSSM.

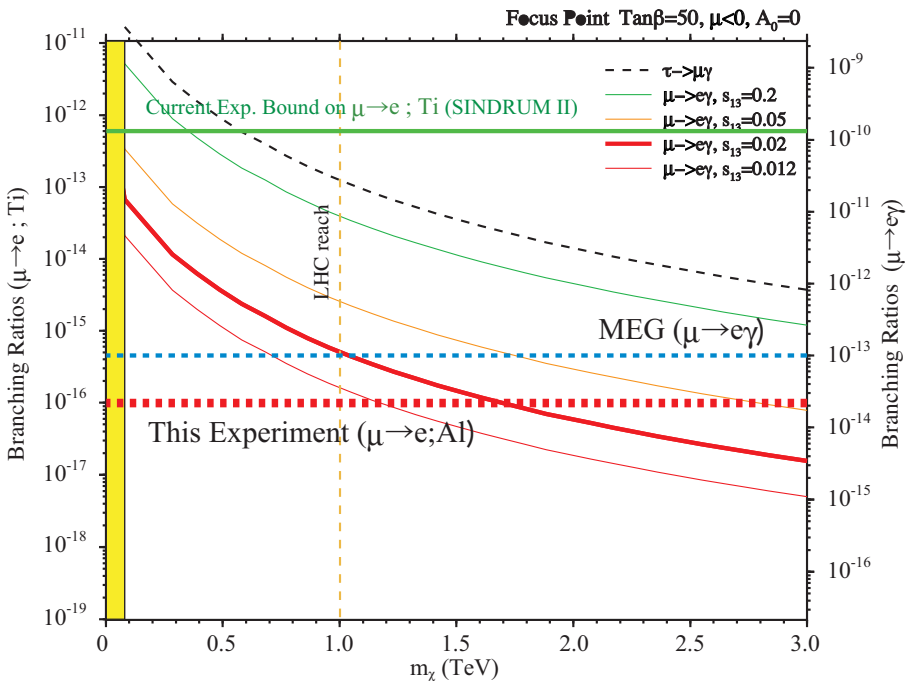

Figure 1.6: Prediction of the branching ratio of MEC in Ti in SUSY-Seesaw models as a function of SUSY mass scale (neutralino). The sensitivity of the proposed experiment is also shown.

TeV, as shown in Fig.1.6. And thereby the search for LFV would be worth carrying out even if LHC does not find SUSY below TeV energy scale.

Chapter 2

Phenomenology of the Muon to Electron Conversion

2.1 What is a $\mu^- - e^-$ Conversion Process ?

One of the prominent muon LFV process is $\mu^- - e^-$ conversion in a muonic atom. When a negative muon is stopped in some material, it is trapped by an atom, and forms a muonic atom. After it cascades down in energy levels in the muonic atom, a muon is bound in its $1s$ ground state. The fate of the muon is then either decay in an orbit ($\mu^- \to e^- \nu_\mu \overline{\nu}_e$) or capture by a nucleus of mass number A and atomic number Z, namely

$$\mu^- + (A, Z) \to \nu_\mu + (A, Z - 1). \tag{2.1}$$

However, in the context of physics beyond the Standard Model, the exotic process of neutrinoless muon capture, such as

$$\mu^- + (A, Z) \to e^- + (A, Z), \tag{2.2}$$

is also expected. This process is called $\mu^- - e^-$ conversion in a muonic atom. It violates the conservation of the lepton flavor numbers, L_e and L_μ, by one unit, but conserves the total lepton number, L.

The branching ratio of $\mu^- - e^-$ conversion can be given by

$$B(\mu^- + (A, Z) \to e^- + (A, Z)) \equiv \frac{\Gamma(\mu^- + (A, Z) \to e^- + (A, Z))}{\Gamma(\mu^- + (A, Z) \to capture)}, \tag{2.3}$$

where Γ is the corresponding decay width.

The final state of the nucleus (A, Z) could be either the ground state or excited states. In general, the transition process to the ground state, which is called coherent capture, is dominant. The rate of the coherent capture process over non-coherent ones is enhanced by a factor approximately equal to the number of nucleons in the nucleus, since all of the nucleons participate in the process.

2.2 Event Signature

The event signature of the coherent $\mu^- - e^-$ conversion in a muonic atom is a mono-energetic single electron emitted from the conversion with an energy of

$$\begin{aligned} E_{\mu e} &= m_\mu - B_\mu - E^0_{rec} \\ &\approx m_\mu - B_\mu, \end{aligned} \tag{2.4}$$

where m_μ is the muon mass, and B_μ and E^0_{rec} are the binding energy of the $1s$ muonic atom and the nuclear-recoil energy respectively. The nuclear-recoil energy is approximately $E^0_{rec} \approx (m_\mu - B_\mu)^2/(2M_A)$, where M_A is the mass of the recoiling nucleus, which is small. Since B_μ is different for various nuclei, the peak energy of the $\mu^- - e^-$ conversion signal changes. For instance, it varies from $E_{\mu e} = 105.0$ MeV for aluminum, $E_{\mu e} = 104.3$ MeV for titanium to $E_{\mu e} = 94.9$ MeV for lead.

From an experimental point of view, $\mu^- - e^-$ conversion is very attractive. Firstly, the e^- energy of about 105 MeV is far above the end-point energy of the muon decay spectrum ($\sim$ 52.8 MeV). Secondly, since the event signature is a mono-energetic electron, no coincidence measurement is required. The search for this process has the potential to improve the sensitivity by using a high muon rate without suffering from accidental background, which would be serious backgrounds for other processes, such as $\mu^+ \to e^+\gamma$ and $\mu^+ \to e^+e^+e^-$ decays.

2.3 $\mu^- - e^-$ conversion and $\mu^+ \to e^+\gamma$

As explained later, there could be two contributions in the $\mu^- - e^-$ diagrams. One is a photonic contribution, and the other is a non-photonic contribution. For the photonic contribution, there is some relation between the $\mu^- - e^-$ conversion process and the $\mu^+ \to e^+\gamma$ decay. Suppose a photonic contribution is dominant, the branching ratio of the $\mu^- - e^-$ conversion process is expected be smaller than that of $\mu^- - e^-$ decay by a factor of α, namely about a few hundred. It implies that the search for $\mu^- - e^-$ conversion at the level of 10^{-16} is comparable to that for $\mu^+ \to e^+\gamma$ at the level of 10^{-14}.

More precisely, this factor depends on the nucleus used in the $\mu^- - e^-$ conversion search[22]. For instance, the factor in aluminum is about 1/400, the branching ratio of $\mu^+ \to e^+\gamma$. With taking account of relativistic atomic effects, Coulomb distortion, finite nuclear size and nucleon distribution, it was found that the ratio of $\mu - e$ conversion to $\mu^+ \to e^+\gamma$ varies from 1/389 for ^{27}Al to 1/238 for ^{48}Ti, and decreases again to 1/342 for ^{208}Pb [23].

If the non-photonic contribution dominates, there is no relation between $\mu^+ \to e^+\gamma$ decay and $\mu^- - e^-$ conversion. It would be worth to note the following. When a $\mu^+ \to e^+\gamma$ signal is found, then a $\mu^- - e^-$ conversion signal has to be found. When no $\mu^+ \to e^+\gamma$ signal is found, there is still opportunity to find a $\mu^- - e^-$ conversion signal if non-photonic contribution exits.

Regarding the non-photonic contribution, it is argued that an extra logarithmic enhancement of the photonic loop diagrams for $\mu^- - e^-$ conversion (and also $\mu^+ \to e^+e^-e^+$) over $\mu^+ \to e^+\gamma$ has also been discussed [24]. It happens only when light charged fermions, to which a photon is attached, are involved in the loop diagrams. Therefore, it could occur for SUSY models with R-parity breaking, but not for R-parity conserving SUSY models or SUSY-GUT models.

2.4 Present Status of the Searches

In this subsection, the present status of the LFV experiments with muons in particular, the searches for $\mu^- - e^-$ conversion and $\mu^+ \to e^+\gamma$ decay are presented.

2.4.1 Experimental status of $\mu^- - e^-$ conversion

Table 2.1 summarizes a history of $\mu^- - e^-$ conversion in various nuclei.

Table 2.1: History and summary of $\mu^- - e^-$ conversion in various nuclei.

Process	90% C.L. upper limit	place	year	reference
$\mu^- + Cu \to e^- + Cu$	$< 1.6 \times 10^{-8}$	SREL	1972	[25]
$\mu^- + {}^{32}S \to e^- + {}^{32}S$	$< 7 \times 10^{-11}$	SIN	1982	[26]
$\mu^- + Ti \to e^- + Ti$	$< 1.6 \times 10^{-11}$	TRIUMF	1985	[27]
$\mu^- + Ti \to e^- + Ti$	$< 4.6 \times 10^{-12}$	TRIUMF	1988	[28]
$\mu^- + Pb \to e^- + Pb$	$< 4.9 \times 10^{-10}$	TRIUMF	1988	[28]
$\mu^- + Ti \to e^- + Ti$	$< 4.3 \times 10^{-12}$	PSI	1993	[29]
$\mu^- + Pb \to e^- + Pb$	$< 4.6 \times 10^{-11}$	PSI	1996	[30]
$\mu^- + Ti \to e^- + Ti$	$< 6.1 \times 10^{-13}$	PSI	1998	[5]

2.4.1.1 The SINDRUM II Experiment

The SINDRUM II collaboration at PSI had carried out experiments to search for $\mu^- - e^-$ conversion in various nuclei. A schematic view of the SINDRUM II spectrometer is shown in Fig. 2.1. It consisted of a set of concentric cylindrical drift chambers inside a superconducting solenoid magnet of 1.2 T. Negative muons with a momentum of about 90 MeV/c were stopped in a target located at the center of the apparatus, after passing a CH_2 moderator and a beam counter made of plastic scintillator. Charged particles with transverse momentum (with respect to the magnetic field direction) above 80 MeV/c, originating from the target, first hit two layers of plastic scintillation arrays followed by two layers of drift chambers, before eventually hitting plexiglass Cherenkov hodoscopes placed at both ends. Charged particles having transverse momentum below about 80 MeV/c were contained inside, and could not reach the tracking region under a magnetic field of 1.2 T. A momentum resolution of about 2.8% (FWHM) for the energy region of conversion electrons was

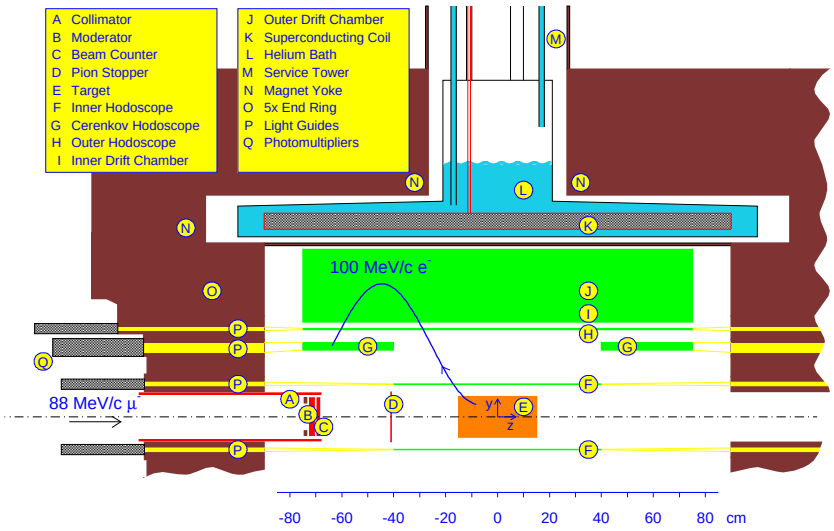

Figure 2.1: Schematic layout of the SINDRUM-II detector.

achieved. For the background rejection the following are used in an off-line analysis: the e^- energy (E_e), a time delay between the times of charged particle tracks in the spectrometer and the beam-counter signal (Δt), the position of the origin of the reconstructed trajectory (Δz) and the polar track angle. Events with small Δt were removed so as to reject prompt backgrounds, such as electron scattering and radiative pion capture.

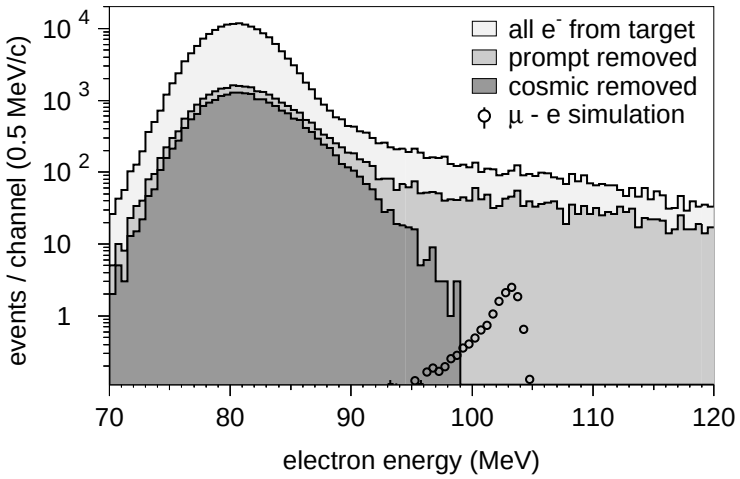

Figure 2.2: Electron momentum distribution for the $\mu^- + Ti \rightarrow e^- + Ti$ reaction, measured by the SINDRUM-II detector.

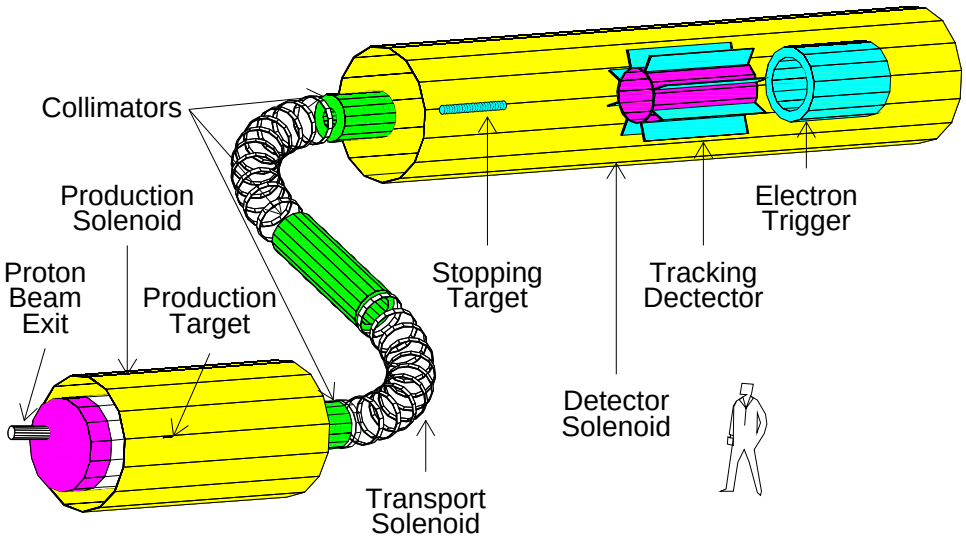

Figure 2.3: Schematic layout of the MECO detector.

In a 1993 run with a titanium target, a total of 3×10^{13} stopped μ^-s were accumulated at a rate of 1.2×10^7 μ^-/s from the $\mu E1$ beam line at PSI. The overall efficiency was about 13 %. The e^- momentum spectrum for the Ti target in the 1993 data is shown in Fig. 2.2, where the successive background rejections by prompt veto (*i.e.* Δt cut) and cosmic-ray suppression are shown. Since no events were found in the signal region, a 90% C.L. upper limit of 6.1×10^{-13} was obtained [5]. Also, for a lead target, it gave $B(\mu^- Pb \rightarrow e^- Pb) < 4.6 \times 10^{-11}$ [30]. Following this work, SINDRUM-II took data with a gold target and those with a lead target in 1997 and 1998, respectively. The data analysis is underway.

2.4.1.2 The MECO Experiment

A new experiment (E940) at Brookhaven National Laboratory (BNL) AGS, called the MECO (Muon Electron COnversion) experiment, was prepared [31]. MECO aims to search for $\mu^- + Al \rightarrow e^- + Al$ at a sensitivity below 10^{-16}. But, it was unfortunate that the MECO experiment was announced to be canceled due to budget problems in summer, 2005.

It will use a new high-intensity pulsed muon beam, which could yield about 10^{11} μ^-/s stopped in a target. A schematic layout of the MECO detector is shown in Fig. 2.3. The MECO apparatus consists of a superconducting (SC) solenoid magnet to capture pions from the production target (production solenoid), a curved transport SC solenoid magnet system (transport solenoid), and a SC solenoid spectrometer, which observes only the 105 MeV signal electrons (detector solenoid). Based on the solenoid capture scheme originally proposed by MELC [32], it has an axially graded magnetic field (from 3.5 T to 2.0 T) to efficiently capture pions from a tungsten target

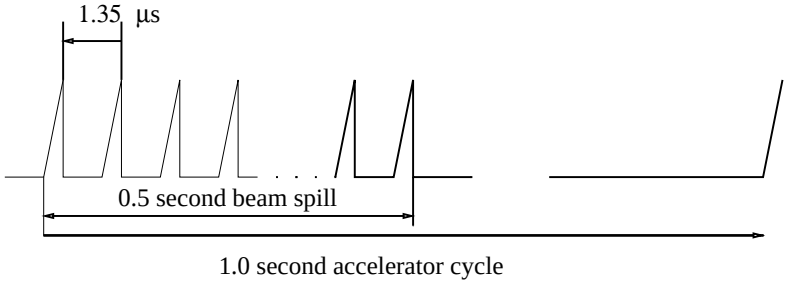

Figure 2.4: Beam spill structure of the MECO experiment.

located on the axis of the solenoid magnet. The curved transport solenoid will capture muons from pion decays, and select the momentum and sign of charged particles by using collimaters at three positions. Layers of thin aluminum targets where the μ^-s are stopped are placed in the detector solenoid with an axially graded magnetic field. The conversion electron of 105 MeV is momentum analyzed with a resolution of 900 keV(FWHM) and an acceptance of 25% in a straw tracking chamber. A pulsed proton beam of about 1 MHz repetition with a pulse length of 30 nsec can be extracted at the AGS. A high extinction between the beam pulses (the ratio of the number of protons between pulses to that in the beam pulse) of 10^{-9} is needed to eliminate severe beam backgrounds at a high rate. They expect to observe 5 signal events for $B(\mu^- Al \to e^- Al) \approx 10^{-16}$ during a one-year run, with an expected background of 0.4 events.

2.4.2 Experimental Status of $\mu^+ \to e^+\gamma$ Decay Search

A experimental search for $\mu^+ \to e^+\gamma$ was carried out by the MEGA collaboration at Los Alamos National Laboratory (LANL). The MEGA detector consisted of a magnetic spectrometer for the positron and three concentric pair-spectrometers for the photon. They were placed inside a superconducting solenoid magnet of a 1.5 T field. The positron spectrometer comprised eight cylindrical wire chambers and scintillators for timing. The positron energy resolution (FWHM) was from 0.5 MeV (0.95%) to 0.85 MeV (1.6%) for a 52.8-MeV e^+, depending on the number of helical loops of e^+ tracks. For the pair-spectrometer, each layer had lead converters, MWPCs, drift chambers and scintillators. The photon energy resolutions (FWHM) were 1.7 MeV (3.3%) and 3.0 MeV (5.7%) for the outer and inner Pb conversion layers, respectively. A surface μ^+ beam of 29.8 MeV/c was introduced along the detector axis, and was stopped in the muon-stopping target made of a thin tilted Mylar foil. All of the charged particles from muon decays were confined within the positron spectrometer. The intensity of the muon beam was 2.5×10^8/sec with a macroscopic duty factor of 6%. The total number of muons stopped was 1.2×10^{14}. By using the likelihood method, a new limit of 1.2×10^{-11} with 90% C.L. has been reported [3]. A new experiment called MEG at PSI, which aims at a sensitivity of 10^{-13} in the $\mu^+ \to e^+\gamma$ branching ratio, is under construction[33]. A schematic view

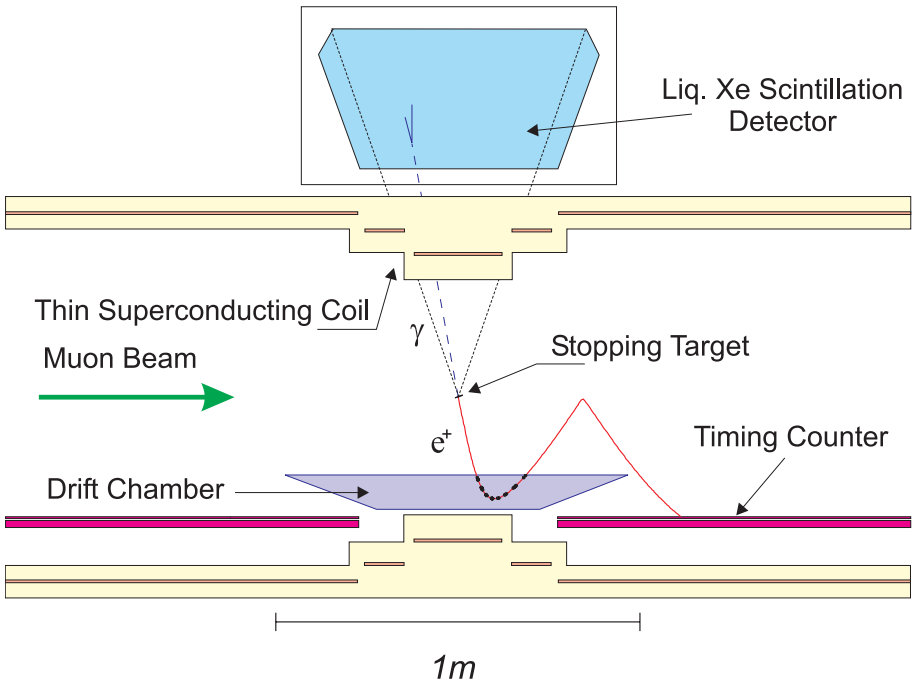

Figure 2.5: Schematic layout of the MEG detector.

of the detector is shown in Fig.2.5. The improvement will be expected by utilizing a continuous muon beam of 100% duty factor at PSI. With keeping the same instantaneous beam intensity as MEGA, the total number of muons available can be increased by a factor of 16. Further improvement is a novel liquid xenon scintillation detector of the "Mini-Kamiokande" type, which is a 0.8-m^3 volume of liquid xenon viewed by an array of a total of 800 photomultipliers from all the sides. The expected resolutions (FWHM) of the photon energy and position are about 1.4% and 4 mm, respectively. As the e^+ detection, a solenoidal magnetic spectrometer with a graded magnetic field is adopted, in which the magnetic field is arranged so that e^+ from the $\mu^+ \to e^+\gamma$ decay follows a trajectory with a constant radius, independently of its emission angle. It allows easier identification of the e^+ in the $\mu^+ \to e^+\gamma$ decay. Physics data taking is expected to start in year 2006 or later.

2.5 Why is $\mu^- - e^-$ Conversion ?

Considering its remarkable physics importance, it is highly desirable to consider a next-generation experiment to search for LFV. There are three physics processes to be considered; namely $\mu^+ \to e^+\gamma$, $\mu^+ \to e^+e^+e^-$, and $\mu^- - e^-$ conversion.

The three processes have different experimental issues to improve their experimental sensitivities. They are summarized in Table 2.2. The processes of $\mu^+ \to e^+\gamma$ and $\mu^+ \to e^+e^+e^-$ are detector-limited. To consider and go beyond the present sensitivities (and presently-aimed sensitivities), detection resolutions have to be improved.

And it is in general very hard. In particular photon energy resolution (which is involved in $\mu^+ \to e^+\gamma$ search) is difficult. On the other hand, for $\mu^+ \to e^+\gamma$ conversion, there is no accidental background and an experiment with higher rates can be doable if a new muon source, which has a higher beam intensity and has a better beam quality to suppress any beam-associated backgrounds, can be constructed.

Table 2.2: LFV processes and issues

Process	Major backgrounds	Beam requirements	Sensitivity issues
$\mu^+ \to e^+\gamma$	accidentals	DC beam	detector resolution
$\mu^+ \to e^+e^+e^-$	accidentals	DC beam	detector resolution
$\mu^- - e^-$ conversion	beam-associated	pulsed beam	beam

Furthermore, it is known that compared with $\mu^+ \to e^+\gamma$. $\mu^- - e^-$ conversion and $\mu^+ \to e^+e^+e^-$ have more physics process to contribute to. Even in SUSY models, the photon-mediated diagrams can contribute to all the three processes, but the Higgs-mediated diagrams can contribute to only $\mu^- - e^-$ conversion and $\mu^+ \to e^+e^+e^-$. In summary, a search for $\mu^- - e^-$ conversion would be a natural next step to go beyond for future improvement.

Chapter 3

Overview of the Experiment

3.1 Overview

We like to present our interest to carry out a new experiment of searching for coherent neutrino-less conversion of muons to electron ($\mu^- - e^-$ conversion), $\mu^- + N(A,Z) \rightarrow e^- + N(A,Z)$, in muonic atoms at a sensitivity of 10^{-16} at the Japanese Proton Accelerator Research Complex (J-PARC). The aimed sensitivity is a factor of 10,000 better than that of current experimental limit[1].

The experiment is planned to carry out in the J-PARC NP Hall by using a bunched proton beam slowly extracted from the J-PARC MR ring. The muon beamline considered consists of high-field pion capture solenoids, curved solenoids to select beam momenta, and a curved solenoid spectrometer to detect $\mu^- - e^-$ conversion with low-counting-rate conditions. A potential layout of the experiment is shown in Fig. 3.1.

To improve the sensitivity by a factor 10,000 from the current limit, several important features have been considered in the proposed experiments. They are highlighted below.

- **Highly Intense Muon Source** : To achieve an experimental sensitivity of 10^{-16}, a total number of muons of the order of 10^{18} muons must be needed, and therefore a highly intense muon beamline has to be constructed. To increase a muon beam intensity, two methods are adopted. One is to use a proton beam of high beam power. J-PARC would offer such a possibility allowing us to use a high proton beam power. The other is to use a system of collecting pions, which are parents of muons, in high efficiency. In the muon collider and neutrino factory R&D, *superconducting solenoid magnets* with a high magnetic field surrounding the proton target has been proposed and studied for pion capture of large solid angle. With the pion capture solenoid system, about 8×10^{20} protons of 8 GeV is needed to achieve the number of muons of the order of 10^{18}.

- **Pulsed Proton Beam** : There are several potential sources of electron background in the energy region around 100 MeV where the signal events from

[1]The current published limit is $B(\mu + Ti \rightarrow e + Ti) = 4.3 \times 10^{-12}$ from SINDRUM-II at PSI [29].

$\mu^- - e^-$ conversion is expected. One of them is beam-related backgrounds. One of the methods to suppress the beam-related backgrounds is a pulsed proton beam by "*beam pulsing*". Since muons in muonic atoms have lifetimes of order 100 nsec, a pulsed beam with beam buckets short compared to these lifetimes would allow one to remove prompt beam backgrounds by measuring in a delayed time window. As will be discussed below, there are stringent requirements on the *beam extinction* during the measuring interval. Tuning of a proton beam in the ring as well as extra extinction devices should be installed to achieve the required level of the beam extinction. And several diagnostic devices for examining the beam extinction should be installed.

- **Muon Transport System with Curved Solenoids** : The pions captured decay to muons, which are transported with high efficiency through a superconducting solenoid magnet system. Beam particles with high momenta would produce electron background in the energy region of 100 MeV, and therefore they must be eliminated with the use of curved solenoids where the centers of helical motions of beam particles drift perpendicular to the bending plane, and the magnitudes of drift are proportional to their momentum. By using this effect and placing collimators, beam particles with high momenta are eliminated.

- **Spectrometer with Curved Solenoids** : To reject electron backgrounds and reduce probability of false-tracking owing to high counting rates, a curved solenoid spectrometer is considered to select electrons by their momenta. The principle of momentum selection is the same as the transport system, but in the spectrometer electrons of low momenta which mostly come from muon decay in orbit (DIO) are removed. The rate of the DIO electrons are about 100 tracks per seconds, whereas the MECO experiment expected hit rates of about 500 kHz per single wire of the tracking device.

3.2 Future Prospects and PRISM

In our previous Letters of Intent, an experiment aiming for 10^{-18} sensitivity with a muon storage ring and a fast extracted proton beam (PRISM) was presented [34, 35, 36]. The R&D works for PRISM are made with Grant-in-Aid. In Appendix, some recent progress is presented. This project needs a new fast-extracted proton beamline and a new experimental facility which we propose. However due to shortage of funding, it will take some time to realize.

This new initiative aiming at 10^{-16} with a bunched proton beam with slow extraction has been taken by our collaboration to achieve an early and timely start of the searches and is regarded as the first step of our staging approach continuing toward the ultimate search and the discovery of $\mu^- - e^-$ conversion. After completing this experiment, further improvements will be sought with the development of PRISM.

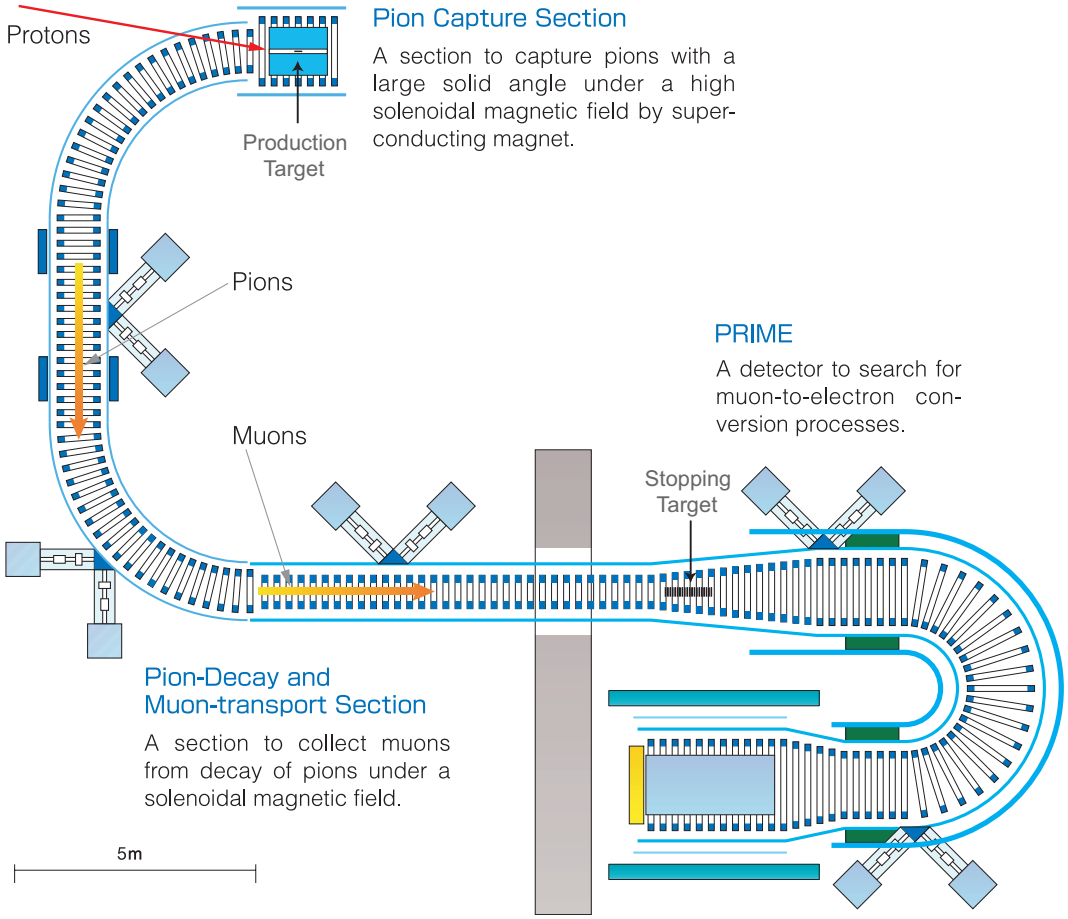

Figure 3.1: Schematic layout of the muon beamline and the detector of searching for $\mu^- - e^-$ conversion. The length of the muon beamline is temporarily set as shown, but it can be adjusted by experimental conditions, such as the location of the detector, etc.

Chapter 4

The Muon Source

4.1 Pulsed Proton Beam

The J-PARC main ring (MR) would deliver a proton beam of its intensity of 3.3×10^{14} protons per cycle with its cycle time of about 0.3 Hz. Protons from the J-PARC MR are extracted either to the Nuclear and Particle experimental hall (NP Hall) by slow extraction, or to the neutrino experimental hall (T2K) by fast extraction. When operated in the slow extraction mode, an average beam current and a duty factor are 15 μA and 0.2 respectively.

The present experiment will be constructed at the NP Hall of J-PARC. The NP Hall will have a slow-extracted proton beam of its maximum energy of 30 GeV and its maximum beam current of 15 μA.[1] The proton beam power will be as much as 450 kW, which would be the strongest in the world among the GeV proton machines. In this section, requirements of a proton beam for the experiment are described.

4.1.1 Proton Beam Power and Energy

Achieving a high sensitivity in searches for rare processes requires high flux of a beam. To accomplish an aimed sensitivity of 10^{-16} in the branching ratio of $\mu^- - e^-$ conversion, about 10^{18} muons in total are needed, as will be discussed in Chapter 6. Based on the current design of the muon beamline, about 8×10^{20} protons of 8 GeV in energy are needed. For a 2×10^7 sec running time, the beam intensity of 4×10^{13} protons per second (which is about 7 μA in beam current) is needed. This requirement on the beam power is about the same as that in the MECO experiment at BNL-AGS [37].

A number of pions (and therefore their daughter, muons) produced by a proton beam is proportional to proton beam power which is given by the product of its beam energy and its beam current. Roughly speaking, as long as the beam power is the same, the pion yield would be almost the same. It is based on the fact that the pion cross section increases linearly as proton beam energy.

[1] In the initial stage, because of lower proton energy at the proton linear accelerator (LINAC), the beam current is expected to be about 9 μA.

It is noted that the reason why low proton beam energy like 8 GeV is considered is two-fold. One is to suppress production of anti-protons as will be discussed in Chapter 6, and the other is the beam extinction where lower beam energy is easier to kick off, as described in Section 4.1.3.

It should be noted that a proton beam from the 3-GeV rapid Cycling Synchrotron (RCS) can not be used. The reasons are the following: (1) The muon facility at the 3-GeV RCS can have a proton target of limited thickness since it is placed upstream from the Neutron facility. (2) Placing a superconducting solenoid for pion capture, surrounding a proton target, as described in Section 4.3, would block muons to the other muon beamline and have potential of conflicts to other muon users. (3) An expected beam intensity of about 10^6 muons/sec, when the concept of pion capture solenoid is given up and the current one target is shared by the other muon beamlines, is too small for our aimed intensity of 10^{11} muons/sec.

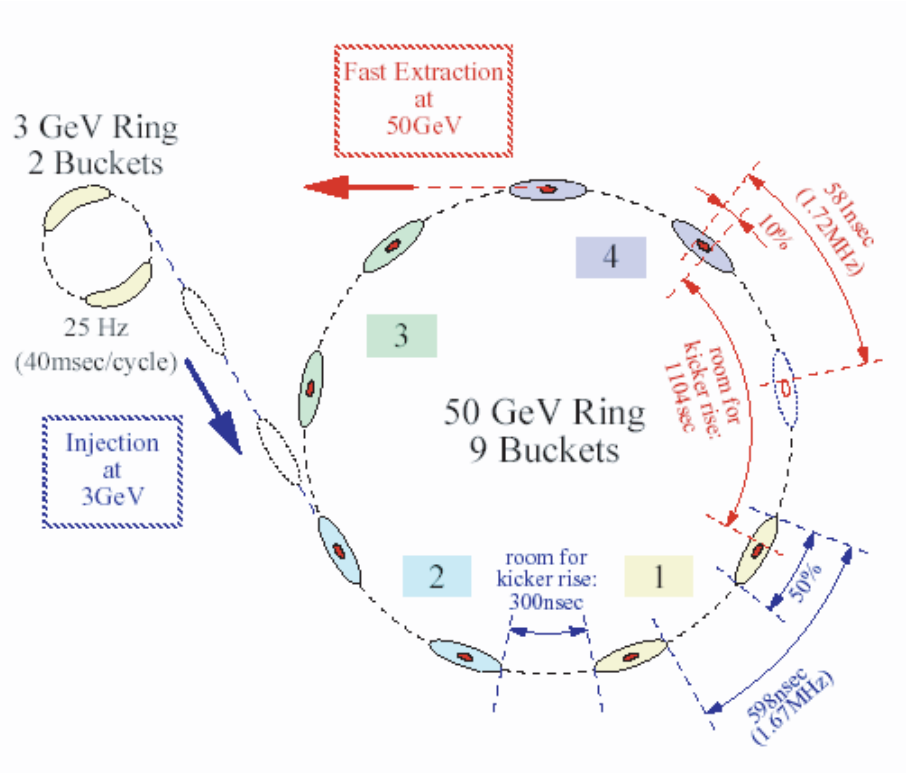

Figure 4.1: Typical machine cycle structure

4.1.2 Proton Time Structure

The cycle time structure of the J-PARC MR is illustrated in Fig. 4.1. Four batches (each of which contains 2 bunches) from the 3-GeV RCS ring are injected into the J-PARC MR when it stays at a low field. When 8 buckets out of 9 are filled with beams, the MR starts acceleration. The time period of every bunch is about 598 nsec

(1.67 MHz) and a gap separation is about 300 nsec (*i.e.* 50 % filling). The present pulse width in the J-PARC Main Ring is 6 nsec in sigma[2].

For the present search for $\mu^- - e^-$ conversion, a proton beam is required to come in bunches with their time separation of about μsec. The detection is carried out between the beam bunches. The time separation of μsec corresponds to a negative muon lifetime, for instance, in Aluminum. This can be done at the J-PARC MR by filling only every other (or every two other) beam bunches in the ring. For instance, the operation of every other mode can be done by filling one of the two bunches in the 3-GeV RCS ring (in a single harmonics operation).

Then, proton bunches in the ring can be extracted in a slow-extraction mode.[3] The proton bunch train in a slow extraction mode is shown in Fig.4.2 This can be possible

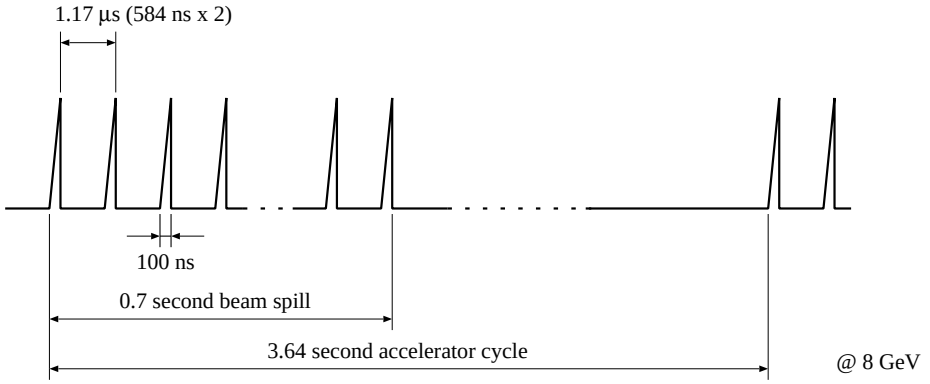

Figure 4.2: Bunched proton beams in a slow extraction mode.

because the debunching rate in the J-PARC MR is slow. It would be also better if we can squeeze a spill length shorter to suppress cosmic-ray induced background.

4.1.3 Beam Extinction

As will be discussed below, the beam extinction between the beam bunches is of critical importance. For the MECO experiment [37], some tests to measure the proton extinction were done at BNL-AGS. In the test, one RF bucket was filled and accelerated to 24 GeV and extracted bunches. And then the rate of neutral kaons with respect to the RF bucket was measured. Figure 4.3 shows the relative intensity as a function of time with respect to the filled bucket. The proton extinction between buckets is below 10^{-6} and in unfilled buckets is of order of 10^{-3}. At BNL-AGS, the second test by using the E787 detector was done to measure the proton beam extinction. They obtained that the extinction of 10^{-7} was measured. They concluded that the proton extinction of 10^{-9} is unlikely to achieve by just tuning of the AGS, and two possibilities to improve the extinction were proposed.

[2]The accelerator people generally use a ± 3 sigma width as a full pulse width. Therefore, this case implies a full width of 36 nsec.

[3]It is more desirable to have single bunch kicking in a fast extraction mode, but it needs large modification of the present extraction scheme. It is considered to be a future plan at this moment.

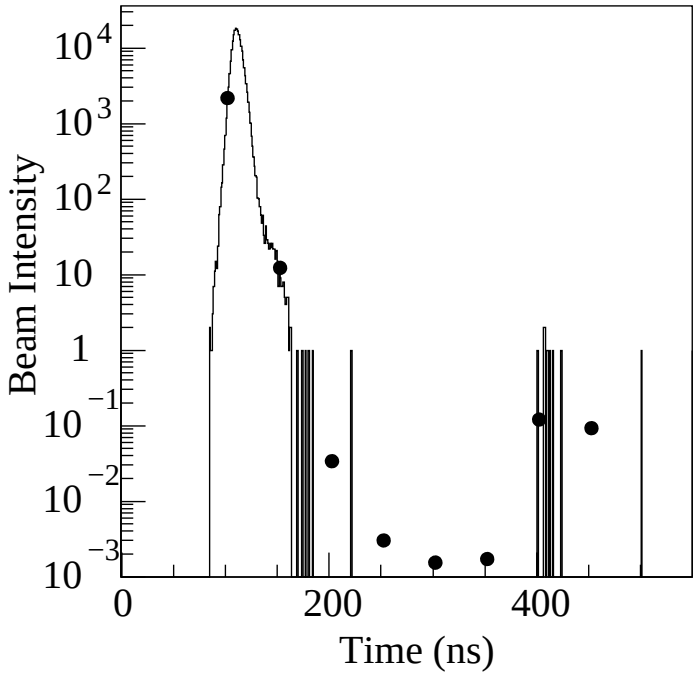

Figure 4.3: Results of the proton beam extinction measured at BNL-AGS. The beam intensity as a function of time with respect to pulses in the bunched beam extracted from the AGS. The solid histogram and dots are the results from the measurements of with a QVT and scalers, respectively.

One is to involve a system of kickers in the ring. This system has an advantage that the kickers run continuously during acceleration and kick beams many times, and therefore the kicking field can be relatively small. They proposed the two magnet system in the AGS ring, one of which is running at a slow frequency (60 kHz for AGS) to destabilize the beam and the other one is running at a fast frequency (740 kHz for AGS) to preserve the stability of the beam in the filled RF bunches. The field integral of this kicker is adjusted to be equal and opposite in magnitude so as that the filled bucket pass through when it fires. The options are (1) combination of AC dipole magnets + strip line kickers or (2) resonant kickers.

The second method is to install a pulsed electric or magnetic kicker in the proton transport line. A kicker could, for example, divert an 8 GeV beam by 2 mrad. The beam would then be focused onto a septum magnet located downstream following the kicker. The beam could be transported to the proton target for pion production during the active cycle of the system. The beam will be dumped on the inactive cycle. The beam extinction can be monitored by measuring the proton flux during off cycle.

At the J-PARC MR, the additional beam extinction devices both in the ring and in the proton transport line are considered to be implemented. We are told that there are sufficient space available to install additional extinction devices in the J-PARC MR. The external kicker in the proton transport line allow a measurement of the beam extinction by measuring the intensity and time structure of the diverted beam

between pulses, where the intensity is rather low and easily measured with a simple counting system.

4.2 Proton Target

4.2.1 Pion Production by Proton Incident

This experiment of searching for $\mu^- - e^-$ conversion uses low energy muons stopped in a muon stopping target. These low energy muons are mostly produced by in-flight decay of low energy pions. The low energy pion production is of most interest. In addition, high energy pions could become potential background sources as will be discussed in the other section, and therefore it is better to eliminate them. In order to study the pion production and pion capture by solenoid, Monte Carlo simulations have been performed by using two different types of hadron codes, namely MARS and GEANT3 with FLUKA. Note that the MARS code is a hadron production code developed at Fermilab.

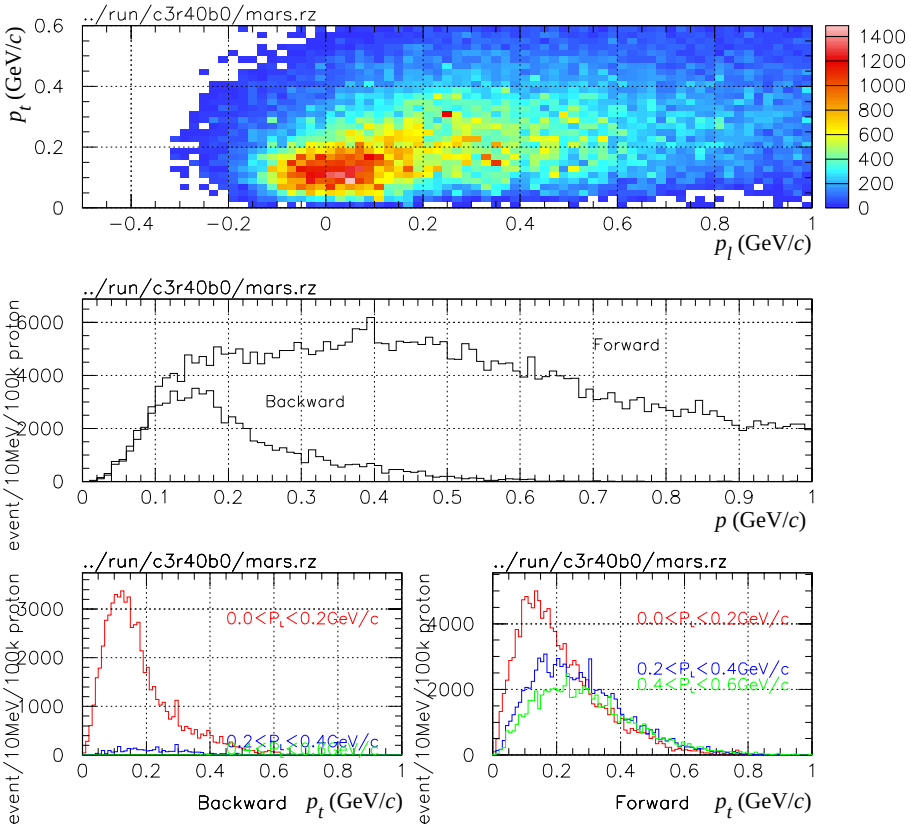

Figure 4.4: Pion production in a graphite target. The top plot shows a correlation between p_L and p_T, and the middle plot shows total momentum distributions of pions going forward and backward π^-s, and the bottom plots show the p_T distributions for $0 < p_L < 0.2$ GeV/c, $0.2 < p_L < 0.4$ GeV/c, and $0.4 < p_L < 0.6$ GeV/c.

Fig.4.4 shows the momentum spectra of π^- produced from a graphite target. The total momentum for the backward pions is peaked at around 120 MeV/c, whereas the peak of forward pion spectrum is around 200-400 MeV/c. It is also seen that high energy pions are suppressed in the backward direction. On the other hand, it is seen that the transverse momenta (p_T) for both the forward and backward pions are peaked around the same 100 MeV/c for low P_L ($0 < p_L < 200$ MeV/c), where P_L is a longitudinal momentum. The low energy pion yields would be not so different between forward- and backward direction. In conclusion, backward pions are less contaminated by high energy pions while retaining the low energy pion yields. From these reasons, we decided to use the backward pions for the present experiment.

Figure 4.5 shows yields of pions and muons as a function of proton energy. As seen in Fig.4.5, the pion yield increases almost linearly as proton energy, therefore by proton beam power. Also it is seen that at a very high proton energy (> 30 GeV), the pion production yield starts to be saturated.

The choice of proton energy can be determined from the pion production yield and the background consideration, in particular of the proton beam extinction and antiproton induced background. At this moment, our choice of proton energy is 8 GeV, as described in Section 4.1. It is the same as in the MECO experiment.

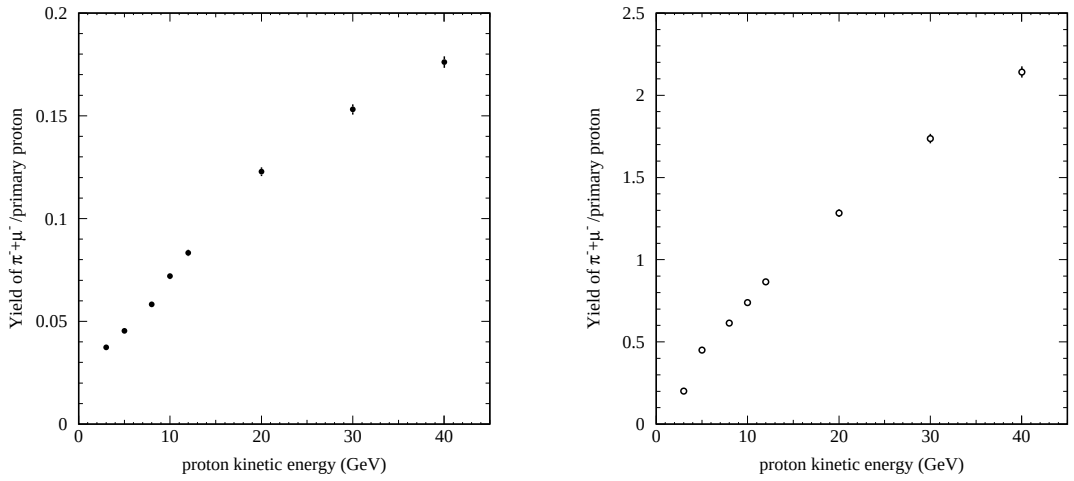

Figure 4.5: Yields per proton of backward pions and muons (in left) and forward pions and muons (in right) from a graphite target in a magnetic field of 5 Tesla as a function of proton energy.

4.2.2 Proton Target for Pion Production

Pion production cross section is higher in a heavier material than a light one; it is almost 3 times larger for tungsten than graphite. However, if it is a metal target, it would melt down when a high power proton beam hits, and therefore target cooling

is necessary. For examples, T1 target in the J-PARC NP hall is designed to be a rotating wheel made of Ni with water cooling.

The proton target for pion production in this experiment will be placed inside the superconducting solenoid magnet. Thus, a rotating wheel target could be adopted. The current target design for this experiment is based on that for T2K experiment; a graphite rod target cooled by He gas. However it is known that replacement of graphite targets in months is needed owing to radiation damage on deterioration of its specific heat. Alternative solution would be the target proposed in the MECO experiment; water cooled tungsten rod, since a proton beam power would be almost the same.

Fig.4.6 shows pion yield as a function of target length. The pion yield at low energy is almost proportional to the target length up to about 60 cm for graphite (which corresponds to 1.5 interaction lengths). Although the longer target provides more pion yields, it should be optimized considering the radiation load to the pion capture solenoid in which the target is embedded. In the current design, the target length is 60 cm.

The yield of pions at low energy decreases as the radius of the target increases. This would be explained by the absorption of pions at low energy. It was found that the optimum radius is about 2 cm for a graphite target. In summary, the target for this experiment will be a graphite target with 1.5 times of the interaction lengths and 2 cm radius, cooled by either water or He gas.

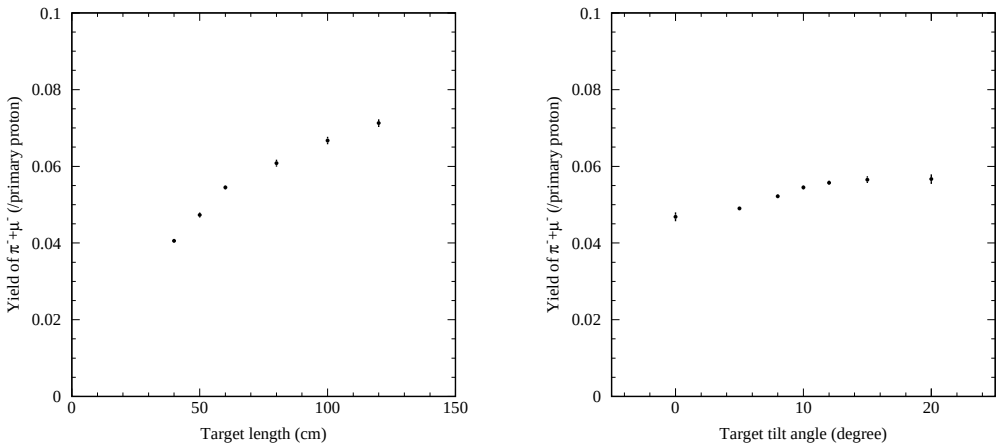

Figure 4.6: Yields of backward pions from a graphite target in 5-Tesla magnetic field as a function of target length (left figure) and target tilt angle (right figure).

Pion production target is embedded in solenoid magnet to capture and transport generated pions in the magnetic field. The target should be tilted with respect to solenoid axis to inject proton beam into solenoid magnet. Figure 4.6 shows the pion yields as a function of tilt angle of a graphite target. As seen in Fig.4.6, the pion

yield is almost saturated around at tilting angle of 10 degree. The deposit energy in a graphite target is 2 kW for 8 GeV protons with 7 μA.

To improve the pion yield, target length, material and position in a solenoid could be replaced to advanced options. If the radiation problem is cleared, a longer target can be used and position can be optimized. A 100 cm graphite target can improve pion yields by 20%. As the target can be placed in the region with decreasing magnetic field, the collection efficiency of pion capture can be improved by 20%. If the cooling technique for heavy metal target is developed, a tungsten target produce 2 times more pions than a graphite target.

4.3 Pion Capture

4.3.1 Pion Capture in a Solenoid Magnetic Field

In order to collect as many pions (and cloud muons) of low energy as possible, they are captured by a high solenoidal magnetic field with a large solid angle. Fig.4.7 shows a layout of the pion capture system, which consists of the pion production target, high-field solenoid magnets for pion capture, and radiation shield. In the current design, only those pions emitted to backward direction are captured if the transverse momentum is less than the maximum, $p_t^{\max}$. This $p_t^{\max}$ is given by a magnetic field strength (B) and the radius of the inner bore of solenoid magnet (R) as

$$p_T^{\max}(GeV/c) = 0.3 \times B(\mathrm{T}) \times R(\mathrm{m})/2. \tag{4.1}$$

The optimisation of the magnetic field of the capture solenoid was performed by

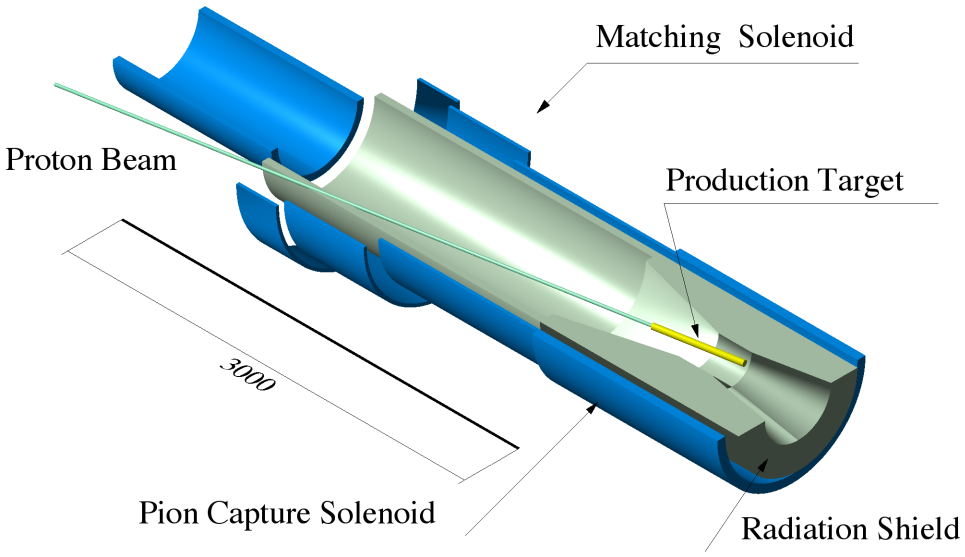

Figure 4.7: Layout of the pion capture system, which consists of the pion production target (proton target), the pion capture solenoid magnets, and its radiation shield.

looking at the muon yields at 10 m downstream from the target; exit of the transport solenoid located at the downstream of the capture solenoid magnet. Note that the most of pions decay into muons in the transport solenoid magnet. It was observed that the higher the pion capture magnetic field is, the better the muon yield at the exit of the pion decay system becomes. Therefore, a higher magnetic field is preferable. According to Fig.4.4, placing $p_T^{\max}$ at around 200 MeV/c would be sufficient. Furthermore, since we are interested in the muon momentum being less than 75 MeV/c, the solenoid magnet with the bore radius of 15 cm can accept most of the parent pions for such low-energy muons. Detailed optimization of the bore radius strongly depends on the available technology of the superconducting solenoid magnet. In the current design, we employ the conservative design values, namely of $B = 5$ T, $R = 15$ cm and the length of 1.4 m.

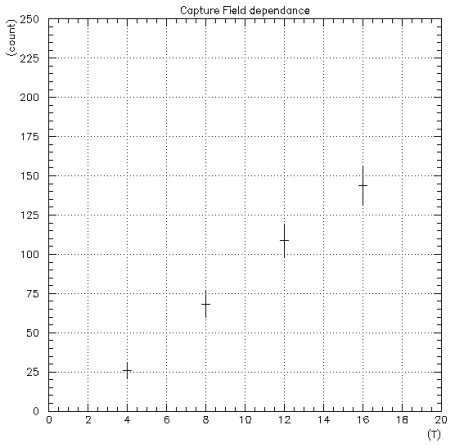

Figure 4.8: Muon yields at 10 m from the entrance of the pion decay system as a function of magnitudes of a pion capture field.

4.3.2 Adiabatic Transition From High to Low Magnetic Fields

Since the pions captured at the pion capture system have a broad directional distribution, it is intended to make them more parallel to the beam axis by changing a magnetic field adiabatically. From the Liouville theorem, a volume in the phase space that beam particles occupy do not change. Under a solenoidal magnetic field, the relation between the radius of curvature (R) and the transverse momentum (p_t) leads to the relation given by

$$p_t \times R \propto \frac{p_t^2}{B} = \text{constant}, \tag{4.2}$$

where B is a magnitude of the magnetic field. Suppose the magnetic field decreases gradually, p_t also decrease, yielding a more parallel beam. This is the principle of the

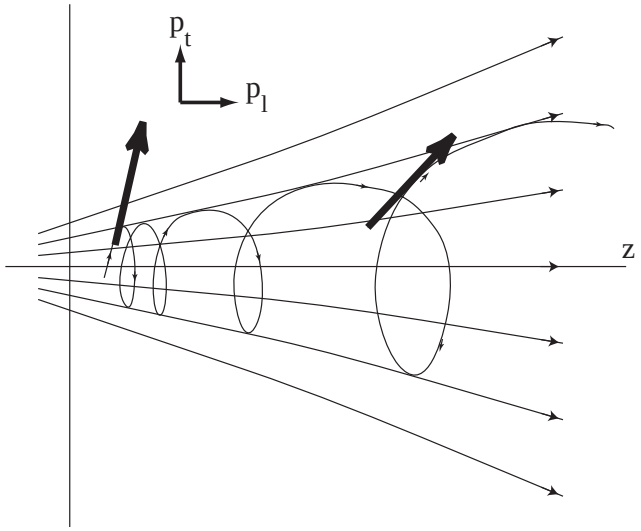

Figure 4.9: Adiabatic transition from a high magnetic field to a low magnetic field. This adiabatic transition reduces the magnitude of transverse magnetic field.

adiabatic transition. Namely, when a magnetic field is reduced by a factor of two, p_t decreases by $1/\sqrt{2}$. On the other hand, since

$$p_t \times R \propto B \times R^2 = \text{constant}'. \tag{4.3}$$

the radius of curvature increase by a factor of $\sqrt{2}$. Therefore, the inner radius of a magnet in the pion decay section has to be $\sqrt{2}$ times that of the pion capture. With the cost of a beam brow up, a pion beam becomes more parallel. Furthermore, it is not effective in reality to have a long magnet with a high magnetic field, and a magnetic field has to be lowered at some point. Fig.4.9 illustrates the principle of adiabatic transition.

4.3.3 Pion Capture Solenoid Magnet

We aim to develop the system that can be operated under 500 W of the heat load. Radiation shield should be installed between the target and the superconducting coil. This will further increase the total radius of the superconducting solenoid magnet. The radiation heat load to superconducting coils placed behind the 30 cm-thick radiation shield of tungsten is the level of 2×10^{-5} W/g for 8 GeV proton beam with 7 μA. The radiation heat comes mostly from neutrons.

If copper is used as the stabilizer of the superconducting coils, a total thickness of the coil might be about 20 cm or more[4], and a total impact on the 4.5 K refrigeration load is over 1 kW. In order to overcome this difficulty, we have started design works using Al-stabilized superconducting coil.

[4]For example, see "MECO Superconducting Solenoid System Conceptual Design Report"[38]

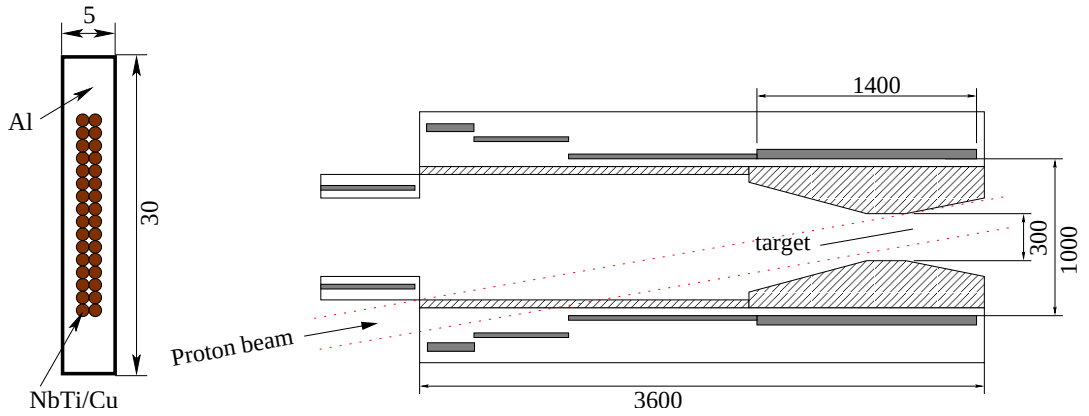

Figure 4.10: (Right) Cross section of superconducting coil for capture solenoid. (Left) Schematic layout of the capture solenoid system. Shaded area is radiation shield made of tungsten. Gray region represents superconducting coil. Proton beam is injected from lower-left of the figure, and captured pions are transported towards left. The unit of the numbers in the figures is cm.

4.3.3.1 Superconducting Coil

To reduce energy deposit by neutrons radiated from pion production target, Al-stabilized superconducting coil is employed. Figure 4.10 shows a cross section view of a coil conductor. It consists of 32 strands of NbTi superconductor with 1.28 mm diameter. The dimension of the conductor is 30 cm in height and 5 cm in width. The fractions of each composition are 19%, 34% and 46% by weight for NbTi, Cu and Al, respectively. The density of the conductor is 4.0 g/cm^3.

4.3.3.2 Layout of Pion Capture Solenoid

Figure 4.10 shows a cross section view of the pion production and capture system. The system consists of pion-capture section with 5-Tesla magnetic field and matching section to the transport solenoid system with 2-Tesla field. The radiation shield is inserted between the pion production target and the coil which generates 5-Tesla magnetic field. To achieve low heat load enough below 100W, 30 cm-thick tungsten shield is necessary. Inner radius of the 5-Tesla coil is 50 cm. The inner bore of the shield is tapered to keep away from beam protons and high energy pions which are scattered forward. To collect backward-scattered pions, proton beam should be injected from the barrel of the solenoid, and should be tilted with respect to the solenoid axis by 10 degrees. The coil near proton beam duct should have larger radius to escape from beam halo. In the current design, the coil is placed more 10-cm far from the beam axis.

The direction backward-scattered pions captured in 5-Tesla magnetic field is focused forward in degrading magnetic field down to 2 Tesla. The matching section has large bore due to increasing diameter of pion trajectory in the tapered magnetic field, and also to contain both the coils of matching and capture section in the large

cryostat.

4.3.3.3 Magnetic Field in Pion Capture Solenoid

To achieve 5-Tesla magnetic field and low radiation heating, the coil is wound in 2 layers, which thickness is only 6 cm in total, and current density in the conductor should be 80 A/mm^2. The magnetic field distribution is shown in Fig. 4.11. The stored energy of the capture solenoid is 12.3 MJ. The ratio of the energy to the mass of superconductor, E/M, is 12.5 kJ/kg, and the critical field is 8.4 T. Therefore, it can be said that the capture solenoid of the design with Al-stabilized superconducting coil is capable with presently achievable technique.

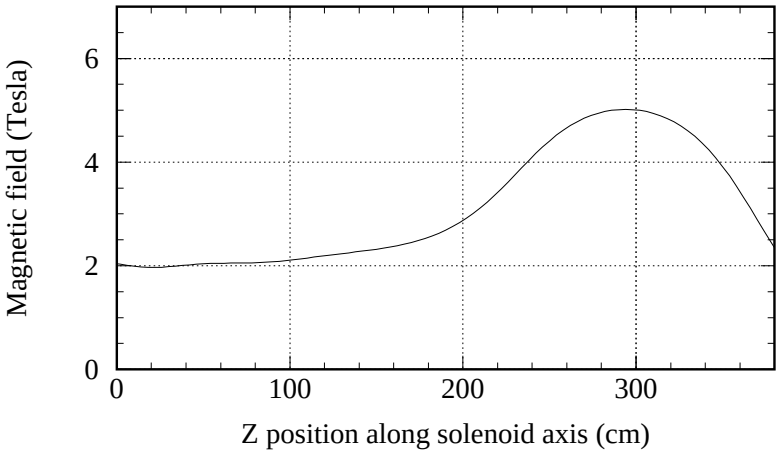

Figure 4.11: Magnetic field along solenoid axis of the pion capture system. Target is located at $z = 300cm$ in the figure, and pions are transported towards left-hand side.

4.3.3.4 Heat Load of Pion Capture Solenoid

From the MARS-simulation study on the radiation shielding, a thickness of the radiation shield made of tungsten should be about 30cm or more, if it is required the heat load on the superconducting coil should be less than 100 W. Figure 4.12 shows the energy deposit distribution in the solenoid system obtained from the simulation. In the current design, deposit energy in the radiation shield around the target is 35 kW for 8 GeV proton beam with 7 μA. Therefore, the shield material should be cooled by water. Heat load on the coil of capture section is calculated to be only 10 W. Since it is well-below our requirements, the coil can be cooled by indirect cooling, which is commonly used for thin superconducting solenoid magnet.

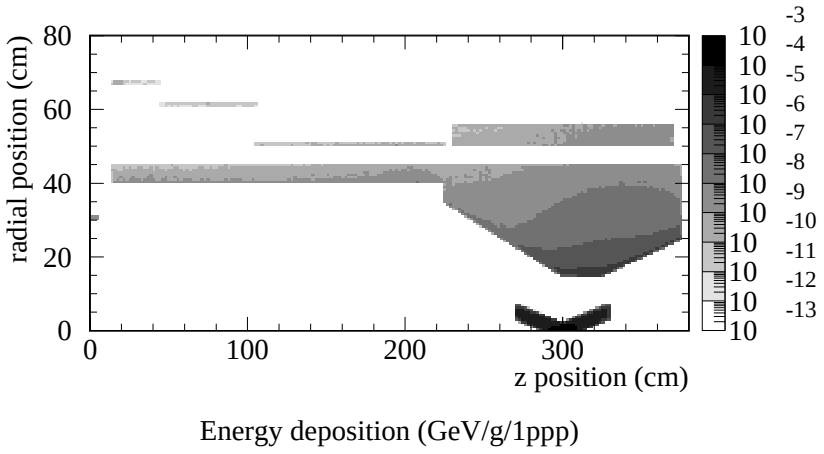

Figure 4.12: Distribution of energy deposit in the materials in the capture system in the unit of GeV/g per proton. The horizontal is z positions along the axis of capture solenoid, and the vertical indicates radial position from the central axis of the solenoids. A graphite target is located at $z = 300cm$ in the figure.

4.4 Muon Beam Line

Pions and muons from the capture solenoid are transported to the stopping target and detector region through a muon beam line, which consists of a curved solenoid section, and a decay solenoid section. An essential point of the beam line is a selection of the charge and momentum. It is necessary to have a high efficiency of transportation for the lower momentum muons around 40 MeV/c, which stop at the stopping. On the other hand, the energetic muons which have a momentum of lager than 75 MeV/c will produce fake signals of $\sim$105 MeV electrons by decaying in flight. Therefore such energetic muons and other unwanted particles are strongly suppressed before the stopping target using the curved solenoid.

A present design of the muon beam line and the magnetic field configuration including the capture section and detector section are shown in Fig. 4.13 and Fig. 4.14. The tracking studies for the solenoid channels were performed using a single-particle tracking code based on "g4beamline" [39]. The magnetic field of the solenoids can be computed from the configuration of coils and their current settings.

4.4.1 Curved Solenoid

To bring pions and muons into the experimental area, a beam has to be bent. Also it is necessary to discriminate the unwanted particles to suppress the detector rate and background rate. These could be achieved by introducing a curved solenoid magnets.

It is known that a center of the helical trajectory of charged particles is drifted in

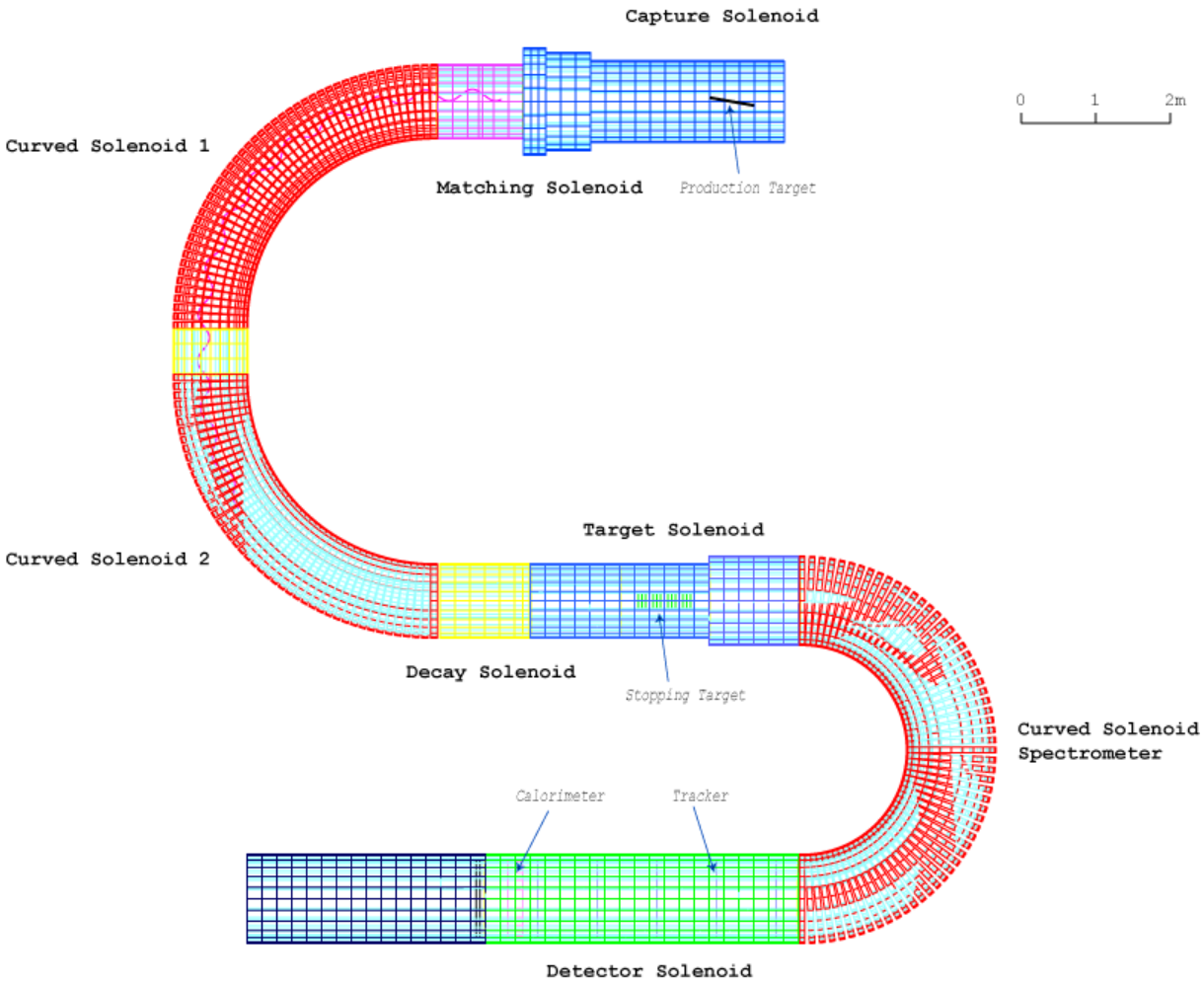

Figure 4.13: Present design of the solenoid channel used in the tracking studies.

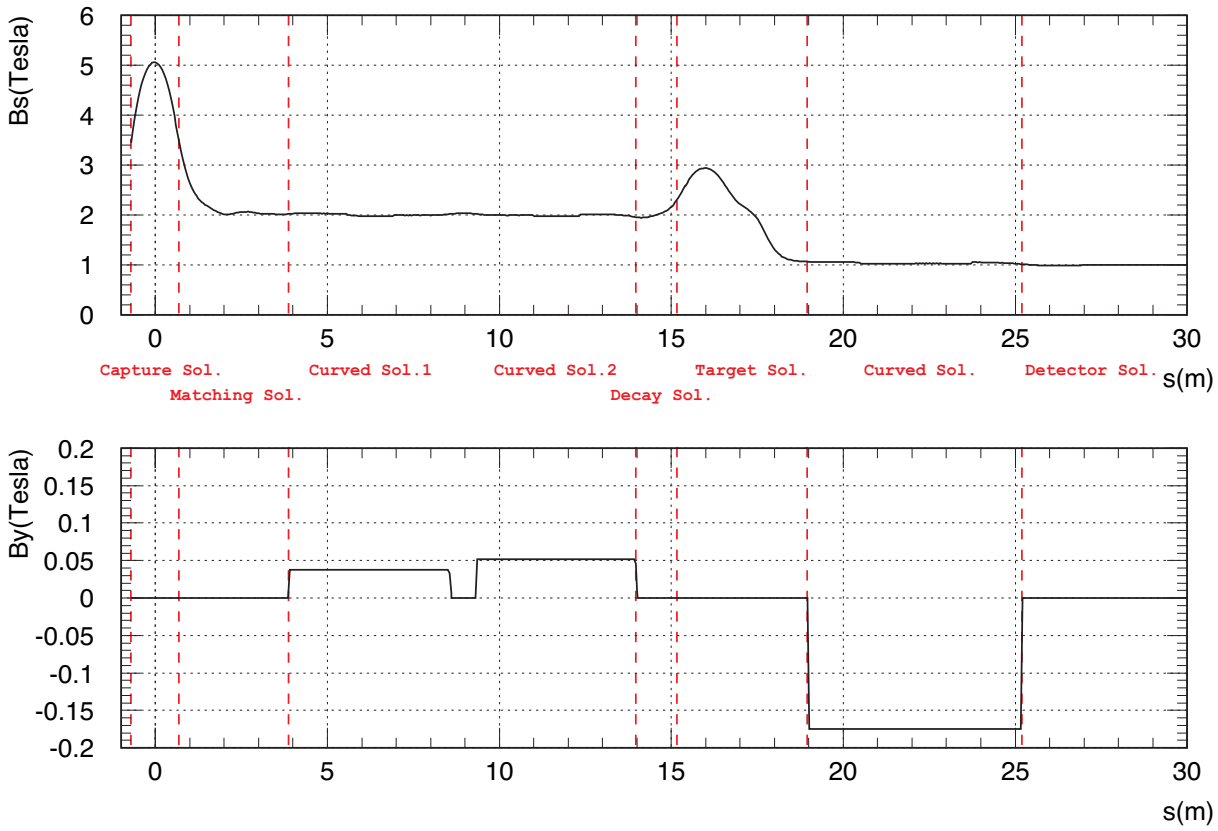

Figure 4.14: The magnetic field configuration of the solenoid channel from the capture section to the detector section of the present experiment. B_s is a central magnetic field of the solenoid magnets. B_y is a correction magnetic field.

a curved solenoid field. The drift (D[m]) is given by

$$D = \frac{1}{0.3 \times B} \times \frac{s}{R} \times \frac{p_l^2 + \frac{1}{2}p_t^2}{p_l} \tag{4.4}$$

where B[T] is a magnetic field at the axis, s [m] and R[m] are a path length and the radius of curvature of a bent solenoid. Namely, s/R is a bending angle. p_l and p_t[GeV/c] are parallel and transverse momentum respectively. Charged particles with opposite sign move in the opposite direction. This can be used for charge and momentum selection if a suitable collimator is placed after the curved solenoid. This kind of curved solenoid magnets have been already adopted in the MECO (BNL-AGS E940) experiment. Unless two curved solenoid of opposite bent are installed, a dipole magnetic field to compensate a drift of the central momentum is needed.

The momentum dispersion is proportional to the bend angle of the curved solenoid. The present design has two curved solenoids with a bend angle of 90° in same bend direction. They have magnetic field of 2 T and curvature radius of 3 m. Reduction of the inner radius of the solenoid works as the collimators and this design would bring down costs. To keep a center of trajectory of the low energy muons, compensative fields of 0.038 T for the first 90° and 0.052 T for the second one was applied. In the tracking simulation these compensative fields are modeled as hard edge fields.

The inner radius are optimized to achieve both of the enough suppression power of unwanted particles and good stopping efficiency of the low energy muons on the target. To determine this parameter a tracking study was performed using a beam data which made by MARS code with 5×10^5 protons on the production target. Figure 4.15 shows the yields of muons passing the beam line, that of stopped muon at the stopping target, and that of muon with higher momentum as a function of the inner radius of the solenoids. The target configuration used in this study is described in a later section. We take the inner radius of 175 mm as a baseline design, which has enough suppression power as mentioned in a later section.

4.4.2 Decay Solenoid

To let pions decay into muons, we need a long flight path. Also to contain those pions and decay muons in a limited space, a long solenoid magnet is required. At the momentum of about 100 MeV/c, a mean decay length of pions is about 10 m, and therefore a flight length of 10 m is needed.

The present design has a straight solenoid of 1.2 meter long between the curved solenoid and the stopping target solenoid section. Therefore a total flight length before the stopping target is about 15 m. Spectrum of particles at the end of the decay solenoid for the inner radius of 175 mm are shown in Fig. 4.16. The pion yield of $1\times10^{-5}\pi$/protons are obtained. It looks like sufficient number in a point of view of a background estimation as shown in a later section.

However, the length of the decay solenoid section depends on the layout of a experimental hall. As shown in Chapter 7, a possible layout in the J-PARC NP-Hall has a long decay solenoid section such as 40 m. Such a long decay solenoid can reject

more pions, while most of muons dose not decay because their lifetime is enough long to survive a several 10 m flight.

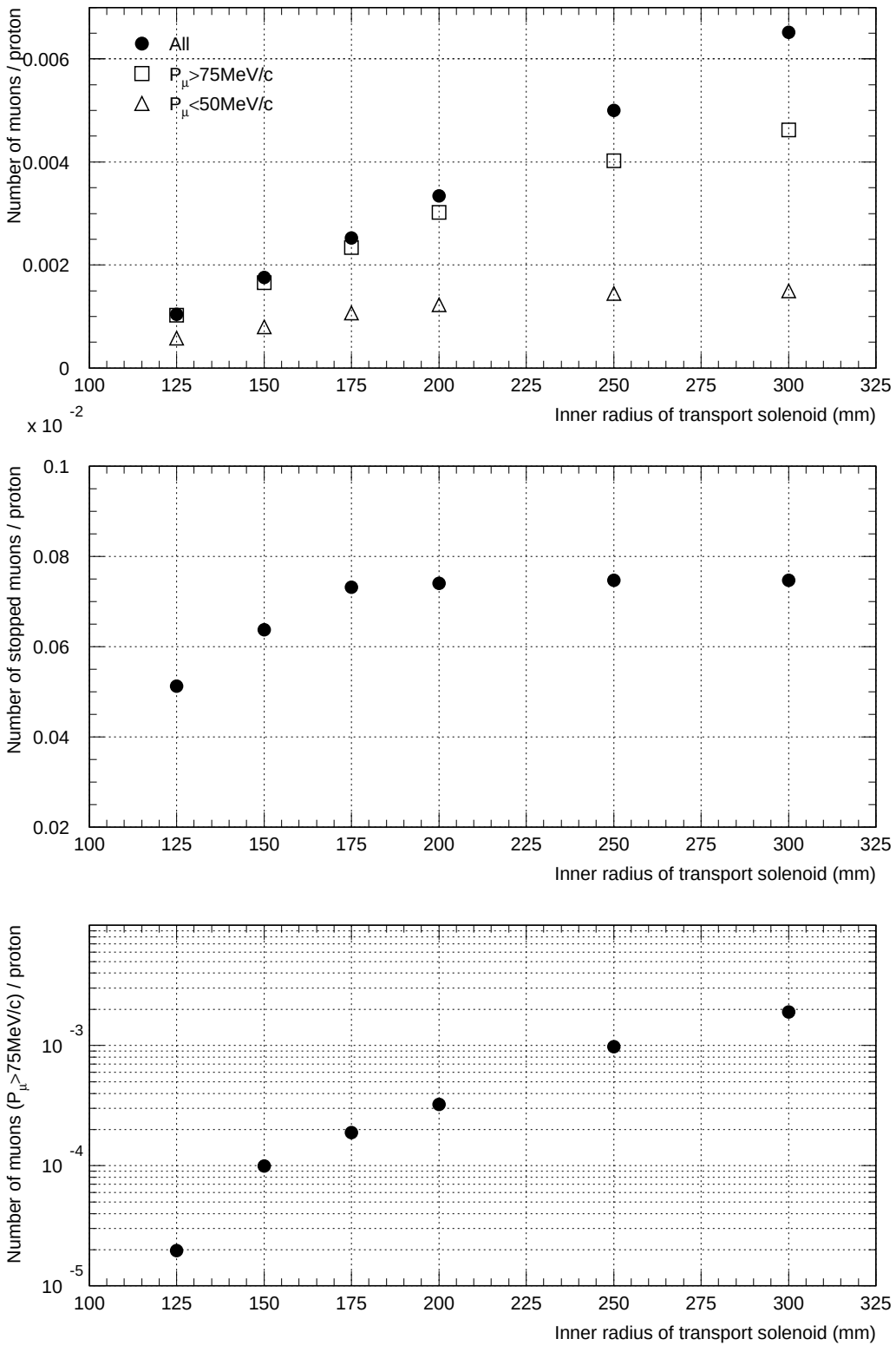

Figure 4.15: The yields of muons passing the beam line (top), that of stopped muon at the target (middle), and that of muon with higher momentum (bottom) as a function of the inner radius of the solenoids

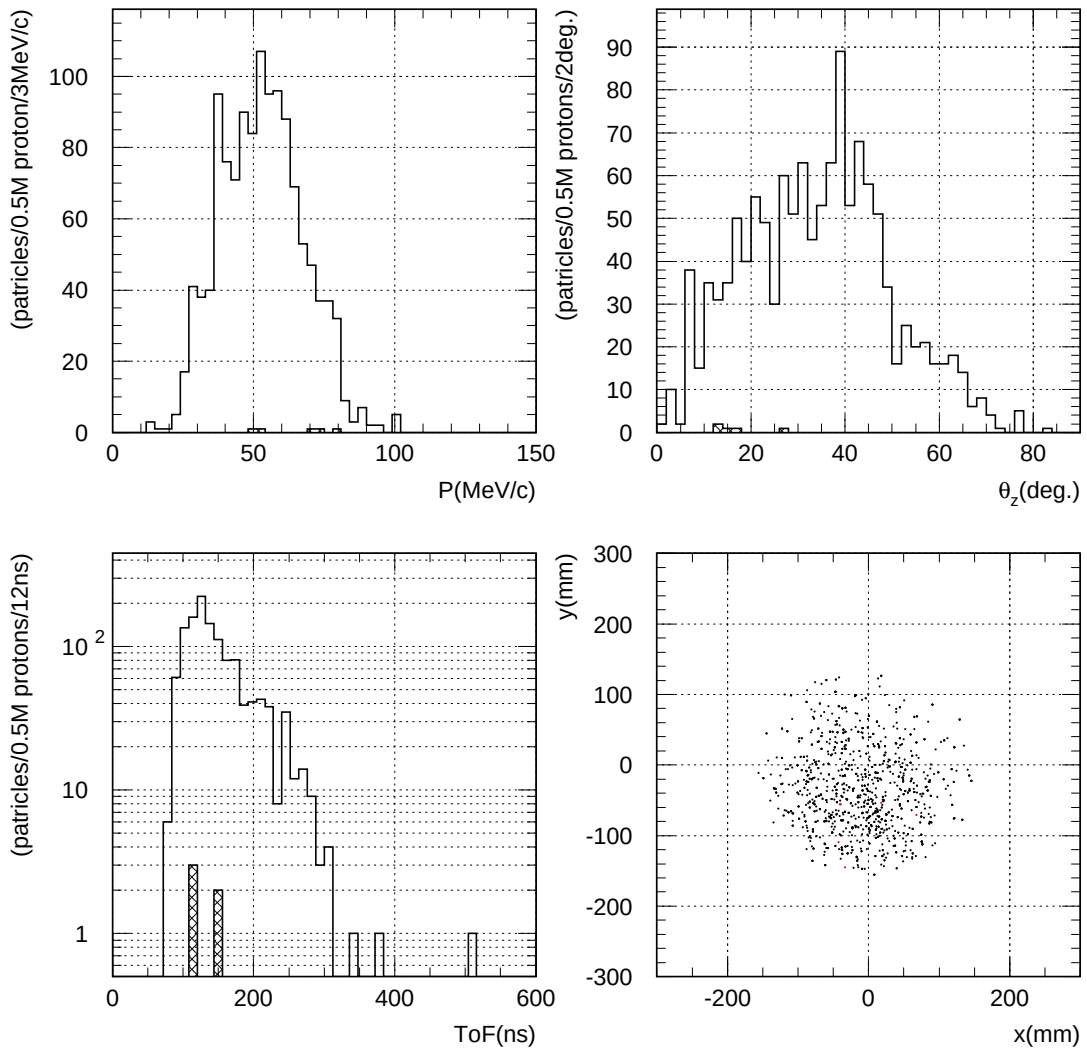

Figure 4.16: Plots for muons and pions (hatched histogram and red markers) at the end of the decay solenoid section. Total momentum (top-left), angle with respect to the axis of the solenoid channel (top-right), time of flight relative to the time when the proton beam hit the production target (bottom-left), and beam profile (bottom-right) are shown.

Chapter 5

The Detector

5.1 Overview

In this chapter, we describe a candidate detector under consideration for searching for $\mu^- - e^-$ conversion at a sensitivity of 10^{-16} in detail. The sole role of the detector is to identify the genuine $\mu^- - e^-$ conversion events from a huge number of background events. The signature of the $\mu^- - e^-$ conversion signal is, as mentioned in Section 2.1, a mono-energetic ($\sim$105 MeV) electron coming from the muon stopping target. By contrast, background events have various origins, and are huge. We will reject backgrounds by various combinations of different methods associated with the muon beamline and the detector. The background rejection will be explained in detail in Chapter 6.2.

The quantities of the signals which can be measured at the detector are only their momentum, energy, and hit timing of electrons. Therefore, to distinguish the signal events from background events, momentum and energy of electrons should be measured as precisely as possible, together with their hit timing with respect to proton bunches.

The detector being considered is quite different from that planned in the MECO experiment [37]. The detector consists of the three sections. The first is the section where a muon stopping target is placed under a graded magnetic field. The second is the section of electron transport with curved solenoid magnets. In this section, electrons and other particles with low energy are eliminated to reduce background rates as well as single counting rates of the detection system follows. The third is the section where momentum and energy of electrons are measured in a uniform solenoidal magnetic field (with a straight solenoid magnet).

5.2 Muon Stopping Target

The muon stopping target must be designed to maximize the muon stopping efficiency and the acceptance of the $\mu^- - e^-$ conversion electron to the spectrometer. Also, it should be designed to minimize the energy loss of the $\mu^- - e^-$ conversion electron as they exit the target in order to improve the momentum resolution of the electrons. It

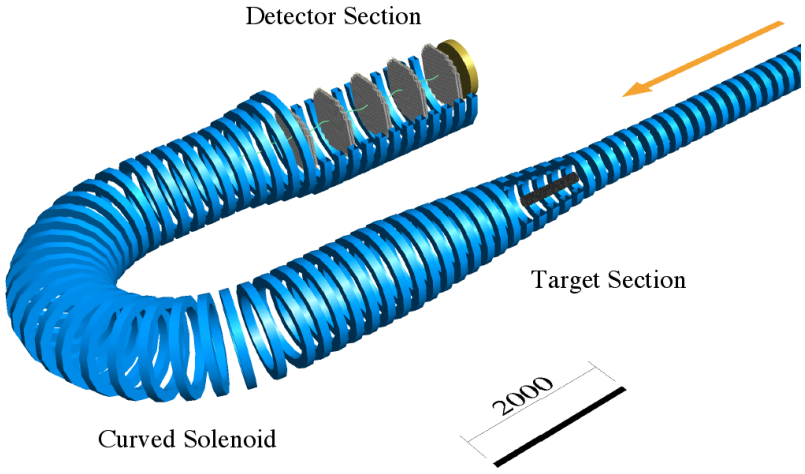

Figure 5.1: Setup of a proposed spectrometer.

would be also important to have the smallest possible target size to reduce any kinds of possible backgrounds.

5.2.1 Choice of $\mu^- - e^-$ Conversion Target

For $\mu^- - e^-$ conversion processes, the branching ratio, $B(\mu^- + N \rightarrow e^- + N)$, has been estimated to increase with an atomic number Z, and then saturate and decreasing with Z. The branching ratio for titanium ($Z = 22$) is larger than aluminum (Z=13) by a factor of 1.7.

In this experiment, to deal with prompt backgrounds and backgrounds due to late-arriving beam particles, a window of detection opens about 700 nsec after the prompt, as shown in Section 5.6. Therefore, it is not suitable to use a heavy material where lifetime of its muonic atom is short. As a result, as in the MECO experiment, it is determined to use aluminum for the $\mu^- - e^-$ conversion target.

Table 5.1: Comparison of different materials of muon stopping targets.

	aluminum	titanium	lead
Atomic number	13	22	82
Lifetime of muonic atoms (μsec)	0.88	0.33	0.082
Relative branching ratio	1	1.7	1.15

5.2.2 Configuration of Muon Stopping Target

The configuration of a muon stopping target is important to improve an experimental sensitivity and remove backgrounds. Major parameters to be considered are material,

thickness, its size (such as a diameter), a number of layers, a distance between disks (spacing), and a magnetic field and its gradient. We have considered various target configurations by GEANT Monte Carlo simulations. Our tentative target configuration is given in Table 5.2.

Table 5.2: Configuration of Muon Stopping Target

Material	aluminum disk
Disk Radius	100 mm
Disk Thickness	200 μm
Number of Disks	17
Disk Spacing	50 mm

It is also important to consider a magnetic field configuration in the stopping target region. A graded magnetic field make a mirror effect, which reflects backward electrons to forward direction, and reduces an poler angle of the electrons at the detector section. The acceptance of the signal electrons ε_{acc} is simply described as

$$\varepsilon_{acc} = \frac{1 - \cos\theta^{crit}}{2}, \tag{5.1}$$

$$\theta^{crit} = \pi - sin^{-1}\left(\sqrt{\frac{B_{target}}{B_{in}}}\right), \tag{5.2}$$

where B_{target} and B_{in} are magnetic fields at and before the muon stopping target respectively. Therefore, the higher B_{in} makes larger acceptance. On the other hand, the maximum poler angle at the detector section $\theta^{max}_{detector}$ is given by

$$\theta^{max}_{detector} = \sin^{-1}\left(\sqrt{\frac{B_{detector}}{B_{target}}}\right), \tag{5.3}$$

where $B_{detector}$ is a magnetic field at the detector solenoid. A larger ratio of $B_{detector}/B_{target}$ is suitable to achieve a good rejection power of the spectrometer solenoid.

Figure 5.2 shows the baseline configuration of the magnetic field at the stopping target region. B_{in} and $B_{detector}$ are set to 3 T and 1 T, respectively. The Al disks of 17 layers are located between 2.43 T to 1.90 T with target radius of 100 mm.

5.2.3 Stopping Efficiency of Muons

A Monte Carlo simulation was carried out with this stopping target configuration to study a stopping efficiency. Momentum distribution of muons at the entrance of the stopping target solenoid and muons stopped on the target disk are shown in Fig. 5.3. The stopping efficiency is 0.29 with this configuration.

5.2.4 Energy Loss of Outgoing Electrons

Figure 5.4 shows energy distribution of the outgoing electrons of 105 MeV/c generated in the muon stopping target, which is simulated by GEANT Monte Carlo simulation. It is found that an average energy loss is about 0.4 MeV.

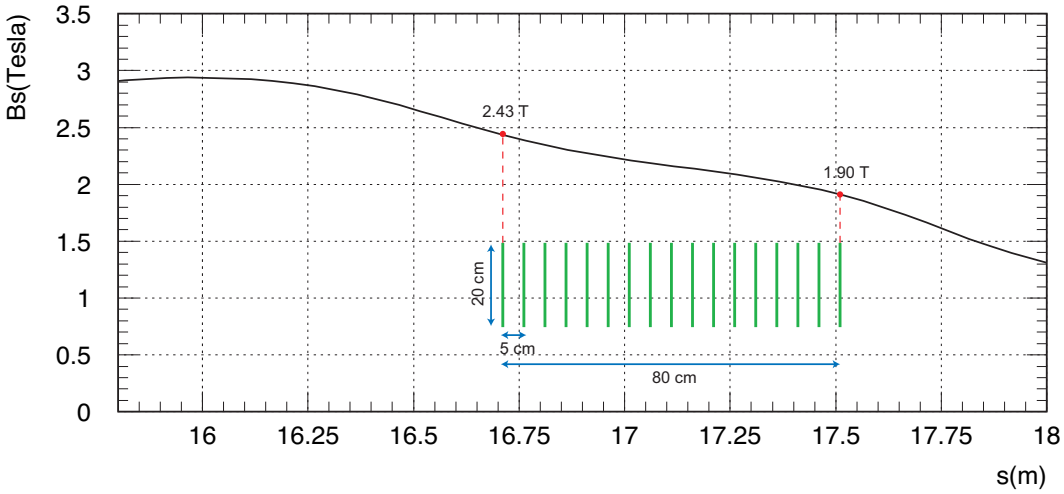

Figure 5.2: Distribution of a magnetic field at the beam axis and the target location.

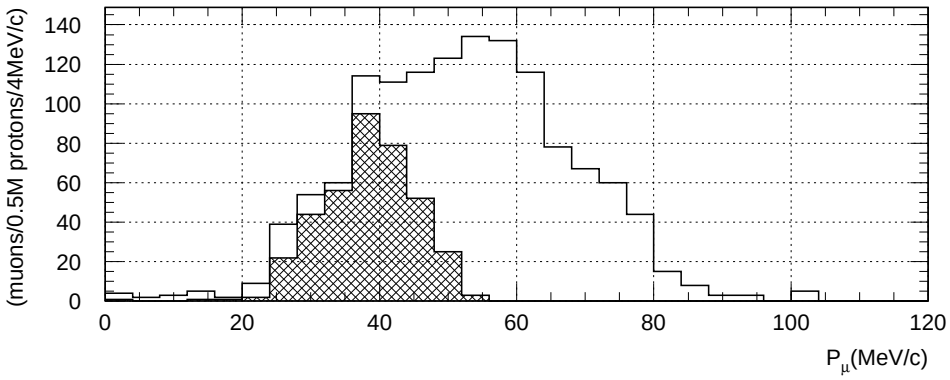

Figure 5.3: Muon momentum distribution at the entrance of the stopping target solenoid. The shaded region corresponds to muons which stop in the stopping target disks.

5.3 Electron Transport with Curved Solenoids

The electron transport system adopts curved solenoid magnets to remove charged particles with low momentum to reject background events as well as to reduce single counting rates of the detection system. The curved solenoid transport system consists of superconducting curved solenoid magnets with collimators inside the solenoid.

Many background particles are generated after the muon stopping target. They come from the stopping in the target, contamination in the beam, and so on. Since these background rate is too high without any reduction, they must be suppressed to work the electron detector. In these backgrounds, electrons from muon decay in orbit (DIO) is the largest background source, and its energy spectrum has distribution to the high energy region near that of the conversion electrons (105 MeV). Fig. 5.5 shows the relation between energy threshold and DIO events with electron energy larger than the threshold energy per one muon stopping in the target. The DIO event rate in the detector region can be reduced greatly by the momentum separator with high energy threshold. For example, expected DIO event for one stopping muon is about 10^{-8} for the energy threshold of 80 MeV as shown in Fig. 5.5. In that case, DIO event rate is reduced to 10^3 Hz for 10^{11} Hz of muons stopping in the target. As a momentum separator, the curved solenoid spectrometer is adopted.

5.3.1 Curved Solenoid and Correction Fields

The curved solenoid spectrometer is a magnetic system to select a charged particle with a desired momentum. Its main features are a large acceptance and a good

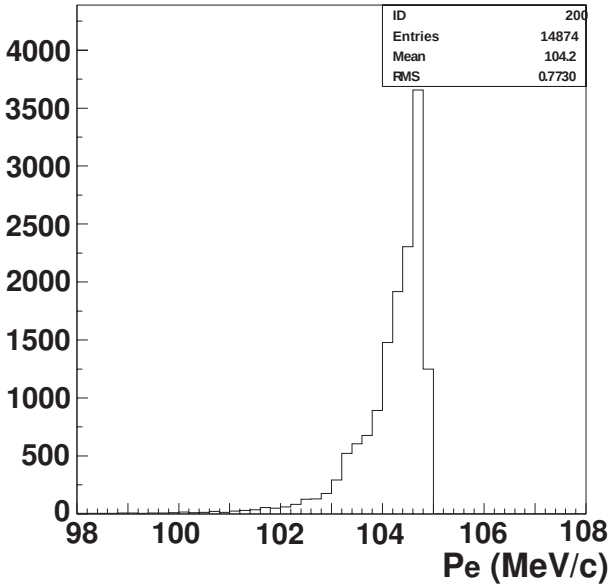

Figure 5.4: Energy distribution of the Monte Carlo events of $\mu^- - e^-$ conversion signals with energy loss in the muon stopping target.

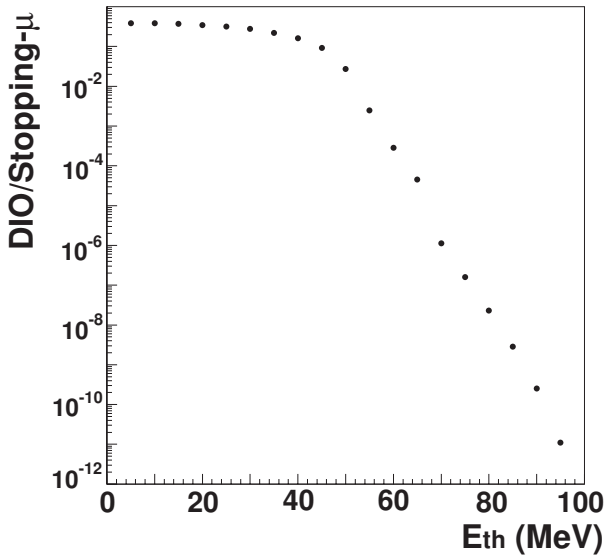

Figure 5.5: Energy threshold v.s. a number of DIO events with electron energy larger than the threshold energy per one muon stopping in the target.

rejection power. In the section, we present the curved solenoid spectrometer itself, and some study results of its performance. First of all, its principle is explained. It is well known that charged particles move in a helical motion around magnetic fluxes in a solenoidal field. When the solenoid is curved, as in a toroidal field, they drift normal to the bending plane. A drift distance D is given by

$$D = \frac{1}{qB_0}\left(\frac{s}{r_0}\right)\left(\frac{p_\parallel^2 + \frac{1}{2}p_\perp^2}{p_\parallel}\right), \tag{5.4}$$

where B_0 represents a magnetic field, r_0 is a radius of the toroid, s is a path length along the particle's central orbit, and $p_\parallel(p_\perp)$ represents respectively particle's parallel (perpendicular) momenta. This drift can be compensated by an auxiliary field imposed along the drift direction. Its value is represented by

$$B_{aux} = \frac{B_0 v_\parallel}{\omega_B r_0}\left[1 + \frac{1}{2}\left(\frac{p_\perp}{p_\parallel}\right)^2\right]$$

with $\omega_B = qc^2B_0/E_e$. For example, if r_0 is set to 2 m, B_{aux}=0.18 T for the signal electron with $\tan\theta = p_\perp/p_\parallel = 0$.

Fig. 5.6 shows an example of tracks in the curve solenoid spectrometer simulated by g4beamline. The track with desired momentum (105 MeV/c) stays in the same horizontal plane, thanks to the auxiliary field, although it undergoes circular motion in the solenoidal field. On the other hand, a track with a wrong momentum (30 MeV/c and 60 MeV/c for example) drifts to the outside of the solenoid. Since the vertical drift distance D depends upon particle's momentum, unwanted particles can be eliminated by placing appropriate collimator inside the solenoid as shown in Fig. 5.6.

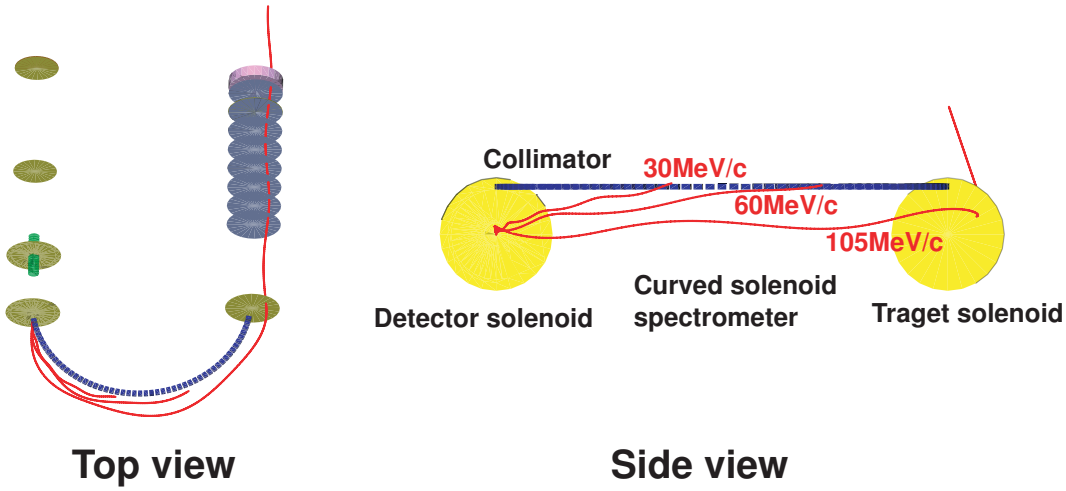

Figure 5.6: Typical tracking events in the electron transport of curved solenoids, simulated by G4beamline. Electrons of 105 MeV/c, 60 MeV/c and 30 MeV/c are emitted with their tilt angles with respect to the beam axis of 15 degrees at the entrance of the curved solenoid spectrometer.

5.3.2 Electron Transmission and DIO Event Rates

The signal acceptance and single event rates were estimated by the "G4beamline" program.[1] The bending angle of the curved solenoid spectrometer (namely, s/r_0 in Eq.(5.4)) of 180 degrees and the applied magnetic field of 1 T are assumed in the g4beamline simulations. A curved collimator whose cross section is rectangular of 5 cm (height) $\times$ 10 cm (width) was placed along the curved solenoid on the upper inside, in the region from 0 degree to 180 degrees in a bending angle. A graded magnetic field from 3 T to 1 T is applied at the target location. The inner radius of the spectrometer solenoid is 50 cm. Figure 5.7 shows the transmission efficiency for electrons generated at the muon stopping target as a function of momentum. From Fig. 5.7, the electron transport system of curved solenoid with these parameters would have a clear momentum selection, where the momentum threshold is about 70$-$80 MeV/c. The transmission efficiency of the signal electrons in the momentum region of 100 MeV/c is about 30 % $-$ 40 %.

Single counting rates of the detectors in the spectrometer is mostly dominated by DIO electrons. To reduce probability of false tracking, single counting rates should be minimized. It is noted that a counting rate of about 500 kHz per single wire in the straw gas chambers in the MECO experiment was estimated. The reduction of DIO electrons by the curved solenoids is estimated by combining the DIO momentum spectrum and the transmission efficiency shown in Fig. 5.7. The performance of rejecting DIO electrons is estimated and is shown in Fig. 5.8 (a), where the survival fraction of DIO electrons as a function of radius of the curved solenoid spectrometer

[1]The G4beamline is a GEANT 4 simulation code developed by the MICE experiment (International Muon Ionization Cooling Experiment) at the Rutherford-Appleton laboratory in the UK.

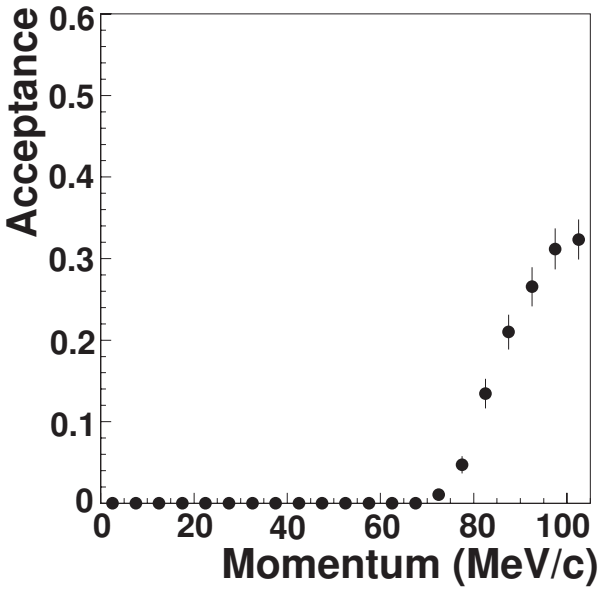

Figure 5.7: Transmission efficiency for electrons from the muon stopping target as a function of momentum. The graded field of 3 T to 1 T is applied to the target region. The inner radius of the spectrometer solenoid is 50 cm.

(which is equivalent to a radial location of the collimator) for various cases of field gradients in the region of muon stopping target. The rejection of DIO electrons can be improved significantly by reducing the solenoid inner radius. For the radius of 50 cm, the surviving rate of DIO electrons of $10^{-7}-10^{-8}$ can be achieved.

The signal acceptance is also investigated by using the g4beamline simulations. Fig.5.8 (b) shows a fraction of the electrons of 100 MeV/c which reach the detector section from the muon stopping target, as a function of radius of the spectrometer solenoids. In Fig.5.8 (b), the signal acceptance of $30-40$ % for field gradients of 3(4) T to 1 T can be achieved, even for small solenoid radius of 50 cm.

The current design of the curved-solenoid spectrometer, in which the bending angle of 180 degrees, and the applied magnetic field of 1T with field gradient in the target region from 3 T to 1 T are planned, would offer the signal acceptance of $30 - 40$ %, and the rejection of DIO electrons of $10^{-7}-10^{-8}$ surviving rates. This curved-solenoid spectrometer would have a capability to reject other charged particles with low momentum. The detector rate is estimated to be an order of 1 kHz for 10^{11} muons in the muon stopping target. The acceptance of the signal event of $\mu^- - e^-$ conversion is about 0.32. Since the geometrical acceptance of the signal events in a graded magnetic field at the target region is about 0.73, the transmission efficiency of the signal events is about 0.44.

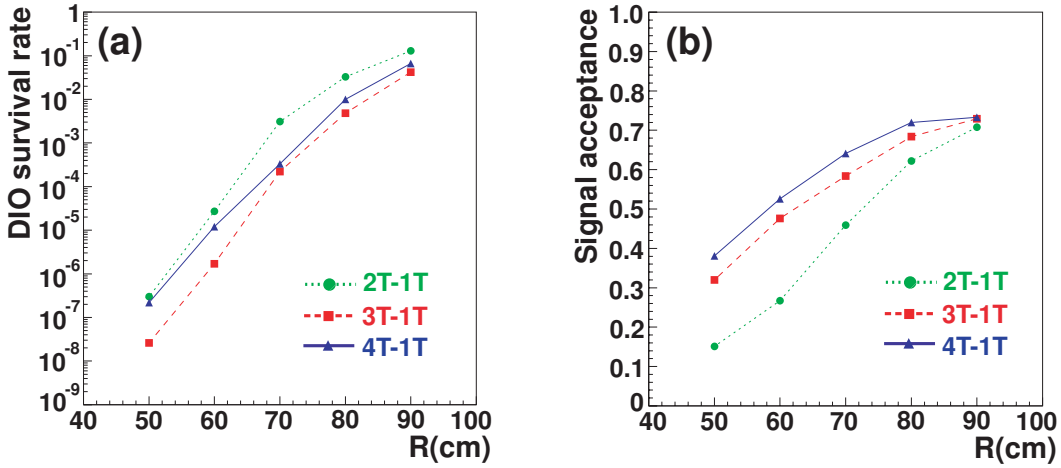

Figure 5.8: (a) Surviving rate of DIO electrons and (b) signal acceptance, as a function of inner radius of the spectrometer solenoid.

5.4 Detection of Electrons

5.4.1 Overview

The main purpose of the electron detector is to identify electrons from other particles and to measure their energies, momenta and timing. It consists of an electron tracking detector with straw gas chambers to measure momenta of electrons, an electromagnetic calorimeter to measure their energies, and fast trigger counters. They are placed under a uniform solenoidal magnetic field for momentum tracking. And also to reduce multiple scattering for momentum measurement, all the system will be placed in vacuum. A candidate layout of the electron detector is shown in Fig.5.9.

Two issues are important when the electron detector is designed. The first issue is single counting rates of the detector. If the counting rate is large, the detector would not be able to distinguish the signal from backgrounds by mistakes in tracking. The second issue is the resolution of electron detection, momentum and energy. From the Monte Carlo simulation, the momentum resolution of less than 350 keV in sigma (or 900 keV in FWHM) is needed.

5.4.2 Electron Tracking Detector

The electron tracking detector is required to measure helical trajectories of electrons in a solenoidal magnetic field with the momentum resolution of less than 350 keV in sigma. Since the momentum of the electrons from $\mu^- - e^-$ conversion is low such as about 105 MeV/c, its intrinsic momentum resolution is dominated by multiple scattering of electrons in the tracker material. Therefore, to reduce a total mass of the tracking detector and to place it in a vacuum are of great importance. For these requirements, a gas wire chamber using straw-tubes, which is strong enough in vacuum, will be used.

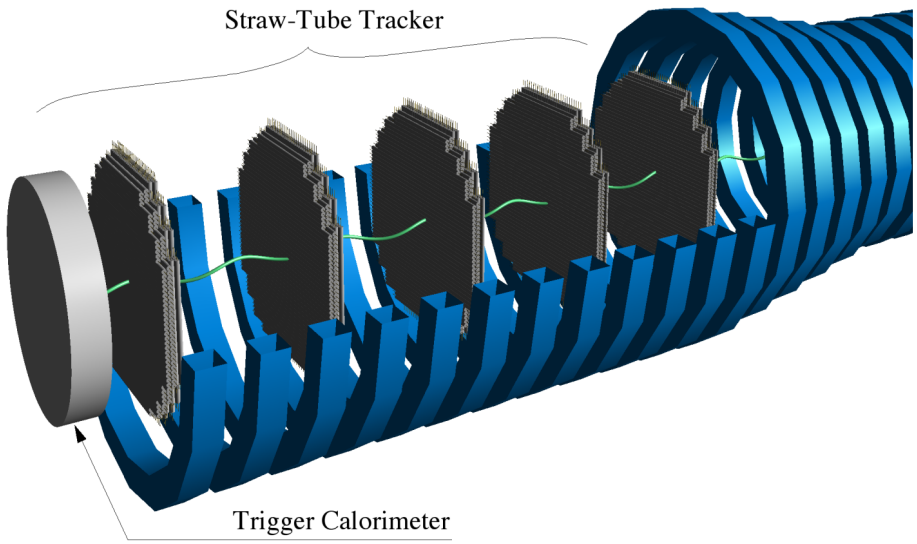

Figure 5.9: Layout of the electron detector. It consists of five layers of straw chambers, followed by an electron calorimetric detector.

The electron tracking system consists of five layers of straw-tube gas chambers. The distance between the layers is set to be 48 cm for all. The locations of the five chambers will be optimized later. Each layer consists of four planes of straw-tube chambers, in which two planes give x-position and the other two planes give y-position.[2] In our current design, a straw-tube of 5 mm in diameter and 25 μm in thickness is being considered. An anode wire is strung at the center of the straw-tube and is applied high voltage and a gas mixture is filled inside the straw-tube. A radial hit position is determined by a drift time of avalanche charges. A prototype chamber was constructed and was tested to study the performance of the prototype chamber by using a π-beam at KEK. As a result, the position resolution of 100 μm was obtained.

The tracker performance including its momentum resolution and reconstruction efficiency, has been studied by GEANT Monte Carlo simulations. The energy and spacial distribution of electrons from the electron transport system were given by the g4beamline simulation code. With this electron information, helical motions in the tracker region were simulated by GEANT 3. In the Monte Carlo simulation, a tracker position resolution of 250 μm was assumed as conservative, although the better position resolution was obtained for the prototype chamber. The momentum reconstruction is performed by χ^2 fitting, assuming the helical motion in a uniform magnetic field of 1 T.

To estimate the effect of multiple scattering in the tracker, the genuine momentum resolution was examined without the tracker material, but only with the position

[2]Another configuration of u, v and w which are rotated about 120 degrees one another is also being considered.

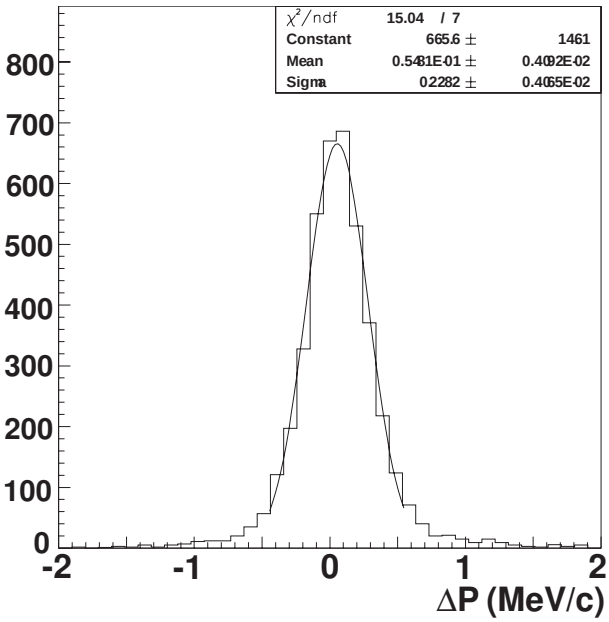

Figure 5.10: Residual distribution between the reconstructed momentum and true momentum.

resolution of 250 μm. The momentum resolution of 50 keV/c in sigma was achieved. Then, simulation calculation was performed with the tracker materials. Fig. 5.10 shows the residual distribution between the reconstructed momentum and true momentum, in which the momentum resolution of 230 keV/c in sigma is obtained. As a result, it is verified that multiple scattering dominate the momentum resolution. And the total mass of five layer straw chambers is small enough to achieve the momentum resolution of 230 keV/c, which meets the requirements of less than 350 keV/c.

The contamination of DIO background into the signal region is estimated by using the events with χ^2 value less than 9.0 to achieve the momentum resolution of 350 keV/c. As a results, the contamination is estimated as 0.05 events after the momentum reconstruction. Therefore, the DIO background by the momentum miss-reconstruction is confirmed to be negligible.

The momentum resolution of 350 keV/c is required to identify the conversion signal from DIO background. The requirement is achieved by the tracking detector using straw-tube chambers. However, DIO background may contaminate into the signal region by miss-reconstruction of the momentum, although the χ^2 function has good value. Therefore, the relation between the momentum resolution and the value of the χ^2 function as shown in Fig. 5.11. From this figure, it is confirmed that the value of the χ^2 function reflects the goodness of the tracking.

5.4.3 Electron Calorimeter

The electron calorimeter, which follows the tracking detector at its downstream, would serves three purposes. One is to measure energy of electrons. High energy resolution

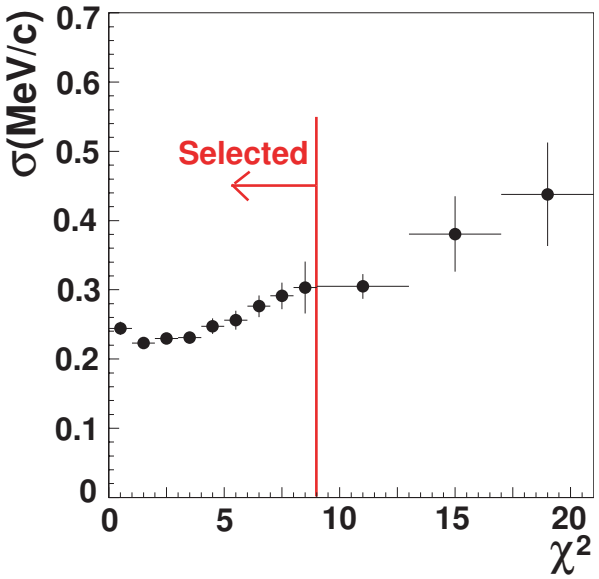

Figure 5.11: Momentum resolution and the value of χ^2 function for the conversion electrons.

is required. The second is to provide a timing signal of the electron events, and at the same time give a trigger signal which could be used to select events to record for further analysis. On this regards, fast response and high efficiency are needed. The third is to give additional hit position of the electron tracks at the calorimeter location. It would be useful to eliminate false tracking.

Redundant measurements of energy and momentum of electrons would be of critical importance to identify the $\mu^- - e^-$ conversion signal events from backgrounds. On this regards, the energy resolution must be very good, and it should have large light yields. Also to reduce a hit overlapped to others, smaller Moliere radius is needed. In addition, fast time response with fast decay constant (< 100 nsec) is required.

We plan to construct the electron calorimeter with cerium doped Gd_2SiO_5 (GSO) crystal. A GSO crystal have a large light yield and a small decay constant, comparing other crystals as shown in Table 5.3. Therefore, GSO crystal is considered a suitable scintillator for the calorimeter. R&D is continued to investigate the basic performance of the electron calorimeter with GSO crystal.

Segmentation would be desired to reduce overlapping. The segmentation would also give an additional hit position which would help reconstruction of the tracks. By comparing the energy (which is measured at the trigger/energy detector) and the momentum (which is measured at the tracking detector) of the tracks, the particle identification can be made. The calorimeter will consists of GSO cells with 3×3 cm^2 cross-section and 11 radiation lengths long (about 15 cm for GSO). If the calorimeter covers the cross-section of the detector region (7850 cm^2), about 900 GSO cells are used. Since that depends on the magnetic field in the detector region and geometry of the calorimeter, it will be optimized by the results of the R&D.

The photon readout from the crystals is one of the key elements for construction

Table 5.3: The characteristics of inorganic scintillator crystals.

	GSO(Ce)	BGO	PWO	BaF_2	CsI(Tl)
Density (g/cm^3)	6.71	7.13	8.2	4.89	4.51
Radiation length (cm)	1.38	1.11	0.92	2.03	1.85
Decay constant (ns)	30-60	300	3	630	1,300
Wave length (nm)	430	480	430	300	560
Light yield (NaI(Tl)=100)	20	7-10	0.26	21	45
Refraction index	1.85	2.15	2.2	1.50	1.79

of the calorimeter. The electron calorimeter is located in vacuum to suppress the multiple scattering in the air. Therefore, low power device must be used for photon readout instead of photo-multiplier. One possible candidate is avalanche photo-diode (APD).

5.5 Cosmic Ray Shield

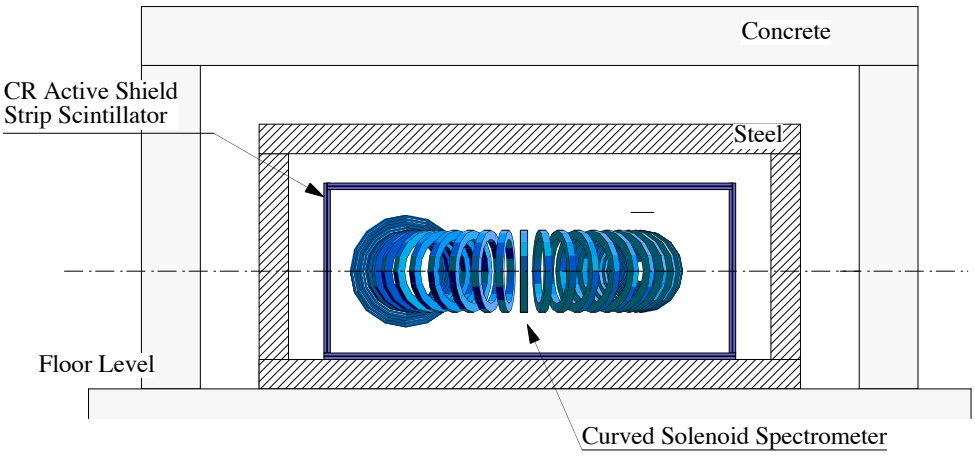

Figure 5.12: Schematic view of cosmic-ray shield.

Cosmic ray induced electrons (or other particles misidentified as electrons) may cause backgrounds. Therefore, passive and active shielding of cosmic rays is considered. Fig.5.12 shows a preliminary layout of the cosmic ray shield. The concrete has a thickness of 1 meters. The passive shielding consists of a combination of steel and concrete wall. The steel enclosure show in Fig.5.12 provides a return path for the detector magnetic field, as well as a passive extra shield against cosmic rays. Steel enclosure has a wall thickness of about 0.5 meters. It is useful to reject low energy muons and electrons from muon decays outside the experimental apparatus. The active shielding will be placed inside the passive shielding, and it covers the whole

electron detector, namely the muon stopping target, the electron transport of curved solenoids and the detector solenoids. The candidate design of the active shielding is two layers of scintillator strips. If it is assumed that the efficiency of each scintillator strip layer to be 99 %, the rejection performance of the cosmic ray background could be 10^{-4}.

5.6 Detection Acceptance

The final acceptance of detection of the $\mu^- - e^-$ conversion signal is determined from the geometrical acceptance of the detector and analysis acceptance by various requirements in offline analysis.

5.6.1 Geometrical Acceptance

Geometrical acceptance and transport efficiency of the spectrometer are estimated as described in the previous sections.

5.6.2 Analysis Acceptance

The analysis acceptance is determined by the requirement on energy of electrons, timing of electrons with respect to proton bunches.

- *Energy :*
  To determine the energy region of the $\mu^- - e^-$ conversion signals, the electrons from $\mu^- - e^-$ conversion were generated inside the muon stopping target by using G3 Monte Carlo simulation. The Monte Carlo events were reconstructed at the tracking detector location, the distribution of reconstructed momentum for the conversion electrons is investigated by G3 Monte Carlo simulation, where the Fig. 5.13 shows the distribution of reconstructed momentum The momentum spread is about 350 keV/c, which includes the effect of energy straggling in the muon stopping target, multiple scattering in the tracker and tracker position resolution. The signal region is assumed to be 104.0 MeV/c to 105.2 MeV/c, which corresponds to one 1.7 sigma width of momentum spread. In this signal region, about 68% of total signal events is contained.

- *Transverse Momentum :*
  To eliminate backgrounds such as beam electrons and muon decay in flight, transverse momentum of electrons greater than 52 MeV/c ($p_t > 52$ MeV/c) at the detector position is requested.

- *Timing :*
  Measurement starts about 700 nsec after the prompt to avoid the beam-related prompt backgrounds. A schematic timing chart is shown in Fig. 5.14. The acceptance in the detection window is about 0.38.

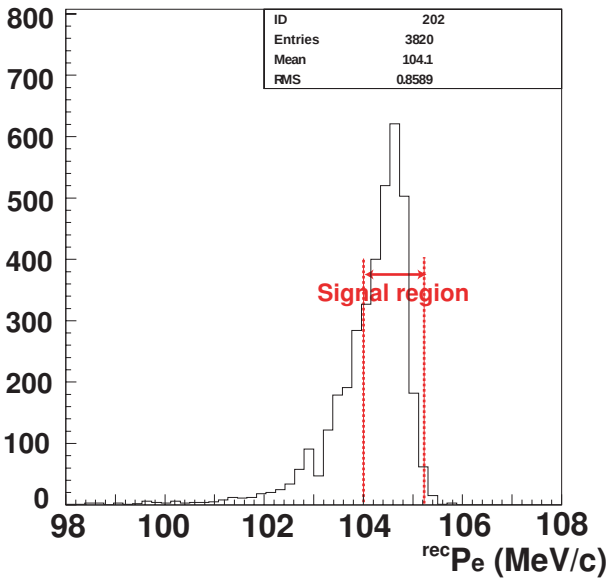

Figure 5.13: The reconstructed momentum distribution of 105 MeV electrons. This is not corrected for average energy loss of electrons (of about 0.4 MeV/c). The energy region for the signal is set to that from 104.0 MeV/c to 105.2 MeV/c for uncorrected energy scale.

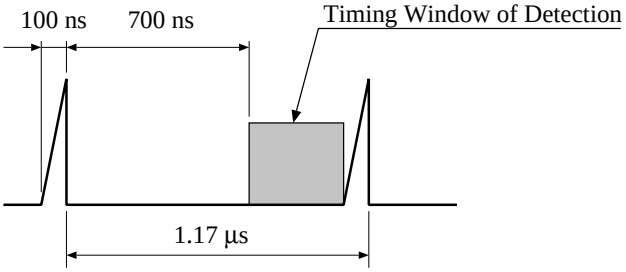

Figure 5.14: Timing window of detection.

5.6.3 Net Acceptance

Table 5.4 summarizes the acceptance at each section. The total signal acceptance at the spectrometer and detector is 0.07.

Table 5.4: The acceptance of the spectrometer and detector.

	Acceptance
Geometrical Acceptance	0.73
Electron Transport Efficiency	0.44
Energy Selection	0.68
Transverse Momentum ($p_t > 52$ MeV/c)	0.82
Timing Window of Detection	0.38
Total	0.07

Chapter 6

Sensitivity and Backgrounds

6.1 Signal Sensitivity

In this section, we estimate a signal sensitivity of our search for $\mu^- - e^-$ conversion. A single event sensitivity is defined by a number of muons stopping in the muon target (N_μ), the fraction of captured muons (f_{cap}), and the detector acceptance (A_e), as follows.

$$B(\mu^- + Al \rightarrow e^- + Al) \sim \frac{1}{N_\mu \cdot f_{cap} \cdot A_e}, \tag{6.1}$$

A total number of muons which are produced and transported through the muon beamline to the muon stopping target (N_μ) of about 5.6×10^{17} for 2×10^7 sec is estimated. It is summarized in Table 6.1. The fractions of captured muons f_{cap} are summarized in Table 6.2. And for aluminum it is about $f_{cap} = 0.6$. The acceptance A_e is summarized as shown in Table 5.4. The total acceptance for the signal is 0.07. By using N_μ, f_{cap} and A_e, the single event sensitivity is obtained by

Table 6.1: A total number of muons delivered to the muon stopping target.

Proton intensity	4×10^{13} protons/sec
Running time	2×10^7 sec
Rate of muons per a proton transported to the target	0.0024
Muon Stopping Efficiency	0.29
Total	5.6×10^{17} stopped muons

Table 6.2: Total muon capture rates in various target nuclei and fraction of captured muons.

	H	Li	Be	B	C	Al	Fe	Cu
rate (10^5 /sec)	0.0045	0.022	0.059	0.28	0.38	6.6	44	57
fraction (%)	0.1	0.5	1.3	5.8	7.7	60.6	90.6	92.6

$$B(\mu^- + Al \rightarrow e^- + Al) = \frac{1}{6 \times 10^{17} \times 0.6 \times 0.07} = 4 \times 10^{-17}. \quad (6.2)$$

Since a 90 % confidence level (C.L.) upper limit is given by $2.3/(N_\mu \cdot f_{cap} \cdot A_e)$, the upper limit is obtained as

$$B(\mu^- + Al \rightarrow e^- + Al) < 10^{-16} \quad (90\% \text{ C.L.}), \quad (6.3)$$

which is about $10,000$ times better than the current published limit obtained by SINDRUM II at PSI of $< 4.3 \times 10^{-12}$ (90% C.L.). [1]

6.2 Backgrounds and Their Rejection

Potential sources of background events for $\mu^- - e^-$ conversion are categorized into three different types of group. They are

1. intrinsic physics backgrounds :
   The intrinsic physics backgrounds originate mostly muons stopping in the muon-stopping target. And they are muon decays in orbit, radiative muon capture, and particles emission after muon capture.

2. beam-related backgrounds :
   This type of backgrounds is caused by particles in a beam, such as electrons, pions, muons and antiprotons. There are two different types, and one is prompt background and the other is late-arriving backgrounds. For the former, the beam pulsing with a high beam extinction is very effective to reject the backgrounds.

3. cosmic ray background.

They will be discussed in details below. Their rejection and remaining background levels are discussed.

6.2.1 Intrinsic Physics Backgrounds

6.2.1.1 Muon Decay in Orbit

When muonic atoms are formed, muons mostly come to its ground state before decaying. Then, they either get captured by a nucleus with emitting a neutrino (nuclear muon capture) or decay in orbit (DIO). For instance, for a aluminum target, about 40 % of muons decay in orbit. The electrons from muon decay in orbit become one of the serious background sources. Their energy spectrum in the energy region lower than 50 MeV mostly resembles the Michel spectrum of ordinary muon decays. However, due to nuclear recoils, a high energy tail exists and extends up to the energy

[1] It is noted that the MECO experiment considered to use a proton target made of tungsten, whereas the present experiment considers to use that of graphite. This causes a difference of the pion yields by a factor of two. If a tungsten target is known to be feasible to use, we will consider that case later.

region of interest for the signal events. One of the way to distinguish the signal events from DIO electrons is to measure the energy of electrons as precisely as possible. As will be discussed below, since the energy spectrum falls sharply as $(E_{\mu e} - E_e)^5$ where $E_{\mu e}$ and E_e are the energy of $\mu^- - e^-$ conversion signal and the energy of electrons respectively, modest detection resolution would be sufficient for their separation.

The energy spectra of DIO electrons are studied with nuclear recoil-energy taken into account [40, 41]. With the approximation of a constant nuclear-recoil energy, the electron spectrum with an expansion in powers of the electron energy (E_e) at the end-point energy is given by

$$N(E_e)dE_e = \left(\frac{E_e}{m_\mu}\right)^2 \left(\frac{\delta_1}{m_\mu}\right)^5 \left[D + E \cdot \left(\frac{\delta_1}{m_\mu}\right) + F \cdot \left(\frac{\delta}{m_\mu}\right)\right] dE_e, \qquad (6.4)$$

where $\delta = E_{\mu e} - E_e$ and $\delta_1 = E_{\mu e} - E_e - E_{\rm rec}$, where $E_{\rm rec}$ is the nuclear-recoil energy given by $E_{\rm rec} = E_e^2/(2M_A)$. The coefficients D, E and F as well as the end-point energy are calculated as shown in Table 6.3 [42, 37]. It should be stressed that the spectrum falls off sharply as the fifth power of δ_1 towards its end-point, $(\delta_1)^5 \approx (E_{\mu e} - E_e)^5$.

Table 6.3: Numerical values of D, E, F and the energy of $\mu^- - e^-$ conversion electrons.

Z	$D(\times 10^{21})$	$E(\times 10^{21})$	$F(\times 10^{21})$	$E_{\mu e}$ (MeV)
13	0.36	0.95	2.27	105.0
22	2.04	6.21	13.28	104.2

To evaluate the background contribution from DIO electrons, their rates and energy spectra have been studied. Since Eq.(6.4) is valid only near the endpoint of the spectrum, the numerical values of the spectrum shapes of DIO electrons complied by Watanabe et al. [43] was used for the low energy region. They are combined and connected smoothly at $E_e = 100$ MeV. Then, the whole spectrum just constructed was scaled to obtain in the unit of the effective branching ratio of $\mu^- - e^-$ conversion[2] Figure 6.1 show the effective branching ratio of DIO electrons as a function of E_e for the case of an aluminum target.

The background rate contributed from DIO electrons is estimated. As described in Section 5.4.2, the momentum resolution of electrons in the tracking system of about 230 keV (FWHM) can be achieved with taking account of the effects of multiple scattering and the position resolution of 250 μm, and a χ^2 cut. From this resolution, the background rate of DIO electrons of about 0.05 events is expected in the signal region which ranges from 104.0 MeV to 105.2 MeV at the sensitivity of 10^{-16}.

[2]The integral of the whole spectrum of DIO electrons is normalized to unity. And then by multiplying a factor of Γ(capture)/Γ(free decay) the spectrum of DIO electrons in an unit of effective branching ratio was obtained as a function of E_e. For an aluminum case, the factor of 2/3 is used.

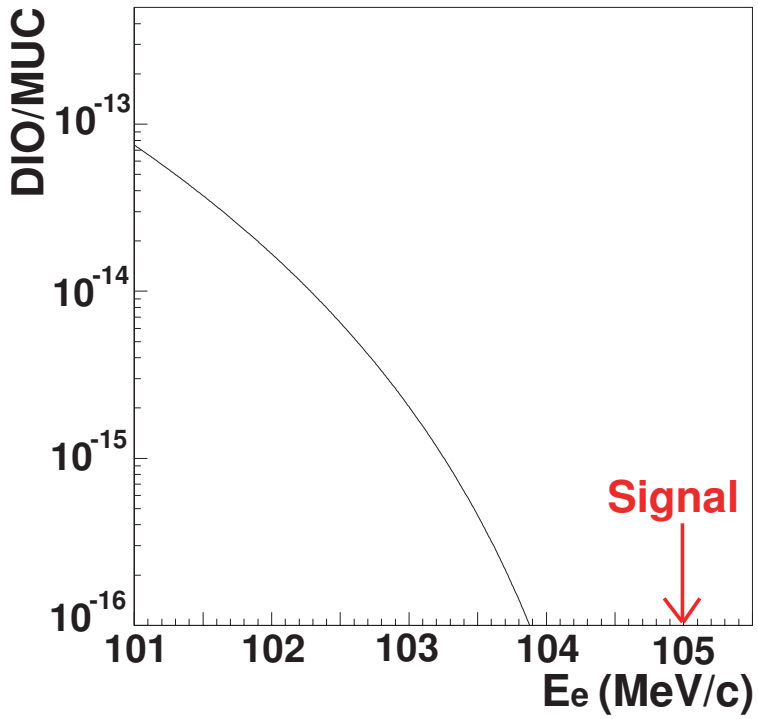

Figure 6.1: Energy spectrum of DIO electrons in a muonic atom in aluminum. The vertical axis shows the effective branching ratio of $\mu^- - e^-$ conversion converted from the DIO decay rate. The goal of this experiment is 10^{-16}.

6.2.1.2 Radiative Muon Capture

Radiative muon capture (RMC), $\mu^- + (A, Z) \rightarrow \nu_\mu + (A, Z-1) + \gamma$, followed by asymmetric e^+e^- conversion of the photon, is another source of intrinsic background events. In an aluminum target, it is $\mu^- + Al \rightarrow \nu_\mu + Mg + \gamma$, where the endpoint of photon energy is 102.5 MeV. The probability per muon capture of producing a photon with energy exceeding 100.5 MeV is about 4×10^{-9} [37]. The conversion probability of photon in the target is about 0.005, and the probability that the energy of the electron produced photon conversion exceeds 100 MeV is about 0.005. Thus, The probability of producing an electron above 100 MeV is about 10^{-13}. These electrons are all less than 102 MeV. Since the signal region from 104.3 MeV to 105.0 MeV is determined, the probability for those events to come in to the signal region is estimated by integrating high energy tail of the resolution function of the tracking system. The probability is evaluated to be less than 10^{-6}. From those, the background rate from RMC is about < 0.001 at the signal sensitivity of 10^{-16}. The background of this type can not be separated, but the measured energy spectrum of electrons can be fitted into a combination of DIO and RMC to estimate each contribution.

Table 6.4: The probability of muon capture with neutrons emission for Si and Ca by the expression of $P(E) = \exp(-\alpha E_n + \beta)$.

	α	β
Si	$-0.096\pm$	-2.970 ± 0.136
Ca	-0.121 ± 0.004	-2.927 ± 0.110

6.2.1.3 Muon Capture with Neutron Emission

When a negative muon is stopped in matter, it is captured in an atomic orbit. It then cascades to the 1s level where it either decays or is captured by the nucleus. As a result of the weak interaction, the latter possibility leads to the following nuclear reaction.

$$\mu^- + N(A, Z) \rightarrow \nu_\mu + N^*(A, Z-1). \tag{6.5}$$

Most of the energy released (≈100 MeV) is carried away by the neutrino. The mean excitation energy of N^* is around 15 to 20 MeV. Thus, N^* can de-excite by emitting one or more neutrons, or charged particles, or it may de-excite via the ordinary electromagnetic mode. They may generate background electrons by the interaction with muon stopping target, solenoid material and so on.

The dominant reaction is neutron emission.

$$\mu^- + N(A, Z) \rightarrow \nu_\mu + xn + N(A-x, Z-1), \tag{6.6}$$

with $x \geq 1$. Together with the electromagnetic de-excitation mode ($x = 0$), these reaction channels account for more than 95% of the total reaction probability.

Inclusive energy spectrum for neutrons emitted after muon capture for Si and Ca is shown in Fig. 6.2, which is measured in Ref. [44]. They are consistent with an exponential dependence on the neutron energy given by the expression of $P(E) = \exp(-\alpha E_n + \beta)$. The fitting results for Si and Ca are summarized in Table 6.4. Since the probability is not much different for materials, the values of Si is used for aluminum.

Background electrons generated by neutrons from muon capture are estimated by GEANT 3 simulation. In this simulation, GCALOR is used as a hadron package. The estimated background contamination into the signal region is less than 0.001.

6.2.1.4 Muon Capture with Emission of Charged Particles

For much less probability than neutron emission, there are reaction channels involving the emission of protons and α-particles.

$$\mu^- + N(A, Z) \rightarrow \nu_\mu + p + xn + N(A-x-1, Z-2), \tag{6.7}$$

$$\mu^- + N(A, Z) \rightarrow \nu_\mu + \alpha + N(A-4, Z-3). \tag{6.8}$$

where (A, Z) is a nucleus with a mass number of A and an atomic number Z. From the cross-section table in Ref. [45], the partial reaction probability of muon capture with

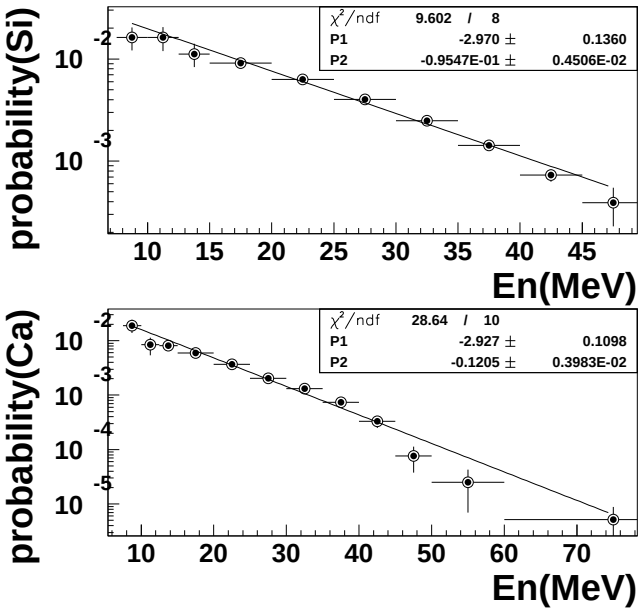

Figure 6.2: Probability of muon capture with a neutron as a function of neutron kinetic energy (E_n) for Si and Ca.

charged particles are plotted against the Coulomb barrier. The classical Coulomb barrier V is calculated as

$$V = \frac{zZ'e^2}{r_0 A^{1/3} + \rho} \tag{6.9}$$

$$V[\mathrm{MeV}] = \frac{zZ}{r_0[\mathrm{fm}]A^{1/3} + \rho[\mathrm{fm}]} \frac{197.3}{137.0} \tag{6.10}$$

where z and Z' are the charges of the outgoing particles and of the residual nucleus, respectively. r_0 is taken as 1.35 fm, and ρ as 0 fm for protons and 1.2 fm for α-particles. For example, V for aluminum is calculated as 5.4 MeV and 7.2 MeV for protons and α-particles, respectively. The probability of muon capture with outgoing charged particles is expressed an exponential function of the Coulomb varier, and the results are summarized in Table 6.5. In Table 6.5, the probability for aluminum and titanium is also shown.

The kinetic energy spectrum of the outgoing charged particles is expressed as

$$P(E_c) = P_0 \exp(-E_c/E_0), \tag{6.11}$$

where P_0 is a normalization constant and E_c is the kinetic energy spectrum of the outgoing charged particles and E_0 is a parameter to determine shape of the spectrum distribution [46]. The E_0 is expressed as a function of Z, which is shown in [46] as a

Table 6.5: The probability of muon capture with outgoing charged particles as a function of $\exp(\alpha V + \beta)$, where V is the Coulomb varier. The probability for Al and Ti is also shown.

Reaction	α	β	Al	Ti
$P(p)$	-0.379 ± 0.017	-3.631 ± 0.187	5.2×10^{-3}	2.5×10^{-3}
$P(pn)$	-0.371 ± 0.022	-1.910 ± 0.186	3.0×10^{-2}	1.5×10^{-2}
$P(p2n)$	-0.383 ± 0.024	-2.104 ± 0.211	2.3×10^{-2}	1.1×10^{-2}
$P(p3n)$	-0.338 ± 0.121	-2.504 ± 1.141	1.9×10^{-2}	1.0×10^{-2}
$P(\alpha)$	-0.460 ± 0.030	-2.203 ± 0.267	7.0×10^{-3}	1.5×10^{-3}

table. Fitting by a linear function, E_0 is determined as,

$$E_0 = 0.03614 \cdot Z + 7.103. \tag{6.12}$$

For aluminum (Z=13), E_0 is obtained as 7.6 MeV.

Background electrons by charged particles from muon capture are estimated by GEANT 3 simulation. In this simulation, GCALOR is used as the hadron package. The background is estimated to be less than 0.001.

6.2.2 Beam-related Backgrounds

6.2.2.1 Radiative Pion Capture

When pions stop in materials, they are immediately captured by a nucleus. About 2 % of the pion captures are associated with emitting photons. It is called radiative pion capture (RPC), $\pi^- + (A, Z) \rightarrow (A, Z-1) + \gamma$. Radiative pion capture followed by internal and external asymmetric e^+e^- conversion of the photon ($\gamma \rightarrow e^+e^-$) would become one of the most serious source of the background. The RPC background can be roughly estimated by the following equation.

$$N_{\mathrm{RPC}} = N_{\mathrm{p}} \cdot R_{\pi/\mathrm{p}} \cdot P_{\pi-\mathrm{surv}} \cdot R_{\mathrm{ext}} \cdot P_{\gamma} \cdot R_{\mathrm{accept}}. \tag{6.13}$$

where N_{p} is a number of delivered protons, and $R_{\pi/\mathrm{p}}$ is a number of pions entering transport solenoid per one proton hitting the production target. $P_{\pi-\mathrm{surv}}$ is pion survival probability in the transport solenoid. P_{γ} is probability of photon conversion in the Al target with a conversion electron in a signal region from 104.0 to 105.2 MeV. R_{accept} is acceptance for signal. R_{ext} is the proton extinction at the off-beam timing.

In this experiment, N_{p} is 8×10^{20}, and $R_{\pi/\mathrm{p}}$ is about 1.5×10^{-2} at 8 GeV operation. All the charge particles should travel the transport solenoid of about 50 m long. Since the momentum is selected to be about 70 MeV/c in the curved solenoid, pions take at least 350 ns to go through the transport solenoid. Therefore, $P_{\pi-\mathrm{surv}}$ is about 1.5×10^{-6}. P_{γ} is less than 3.5×10^{-5}, according to GEANT 3 simulations. R_{accept} is 0.18 and R_{ext} is assumed as 10^{-9}. As a result, the estimated background rate at sensitivity of 10^{-16} is about 0.12 events.

The second contribution to RPC comes from late-arriving pions which take a very long time to traverse and arrive at the muon-stopping target very late. For those events, the proton extinction does not apply for the rejection. However, since the detection window starts about 700 nsec after the proton pulse, those pions lives long, of about 700 nsec. The surviving probability for those late arriving pions per proton of 0.4×10^{-17} which should be substituted for the product of $(P_{\pi-\mathrm{surv}} \cdot R_{\mathrm{ext}})$ in Eq.(6.13). As a result, the expected of RPC background of this type is about 0.002 events. This type of background is easily monitored. By measuring a number of energetic electrons as a function of time during the pulse, the detection window can be appropriately examined.

6.2.2.2 Muon Decay in Flight

Muons decaying in flight can produce energetic electrons that have sufficient total momentum (of about $p_{\mathrm{total}} > 102$ MeV/c) and transverse momentum (of about $p_t > 52$ MeV/c). For the decay electrons to have $p_{\mathrm{total}} > 102$ MeV/c, the muon momentum must exceed 77 MeV/c ($p_\mu > 77$ MeV/c). A Monte Carlo simulation has been done to estimate the yield of muons of $p_\mu > 77$ MeV/c transported through the muon beamline, and it is about 2×10^{-4} per incident proton. The probability for muons to decay in flight in the muon beamline is about 3×10^{-2}. And the probability having an electron energy of 103 MeV/$c < p_{total} <$ 105 MeV/c, and $p_t > 52$ MeV/c is less than 10^{-8}. With the beam extinction of 10^{-9}, the total background level from muon decay in flight is less than 0.02.

6.2.2.3 Pion Decay in Flight

Beam pions decaying to electrons ($\pi \rightarrow e + \nu$) are also a potential source of background. The π momentum must exceed 60 MeV/c to make this background process. A GEANT 3 Monte Carlo simulation was done to estimate the probability of pions with $p_\pi > 60$ MeV/c passing though the muon beamline solenoids. It is noted that the muon beamline has capability to transport beam particles whose momentum are less than about 80 MeV/c. The probability is about 5×10^{-6}. The branching ratio of $\pi \rightarrow e+\nu$ is about 1.0×10^{-4}. The probability of the decay electron from $\pi \rightarrow e+\nu$ to have $E_e > 102$ MeV and $p_t > 52$ MeV/c is about 5×10^{-6}. With the beam extinction factor of 10^{-9}, the background level from pion decay in flight is less than 10^{-3}.

6.2.2.4 Beam Electrons

If electrons in a beam are scattered at the muon stopping target into the detector, they might become background events. The muon beamline is designed to pass beam particles whose momentum is less than 80 MeV/c. By using a GEANT 3 Monte Carlo simulation, the probability of beam particles of 100 MeV/c being transported through this beamline is less than 10^{-8} (statistically limited). Then, the probability for electrons of about 100 MeV in energy from the muon beamline to be scattered off in the target and have a transverse momentum exceeding 52 MeV/c is about 10^{-5}

per proton. With 8×10^{20} protons and the beam extinction of 10^{-9}, the expected background rate of beam electrons is 0.08.

6.2.2.5 Neutron Induced Background

Background induced by neutrons in a beam with high kinetic energy coming through the muon beamline is estimated. Those neutrons could pass through the muon beamline by being kept reflecting its inner sides. The neutrons which can produce electrons of 100 MeV must exceed its kinetic energy of 100 MeV. The rate and energy distribution of neutrons whose kinetic energy is more than 100 MeV/c were examined by MARS simulations. It is about 3×10^{-7} neutrons/proton. And by using GEANT 3 Monte Carlo simulation, an average transit time of those neutrons arriving at the muon stopping target is estimated and it is about 300 nsec, and much less than the waiting time of 700 nsec before detection window opens. Therefore, it is regarded as a prompt background. By using GEANT 3 Monte Carlo simulation, the probability for those neutrons to produce electrons of about 100 MeV in energy was estimated and found to be about 10^{-7}. With the beam extinction of 10^{-9}, the background rate of neutron induced of this type is about 0.024.

6.2.2.6 Antiproton Induced Background

Another potential source of background is induced by antiprotons. Owing to the momentum selection of the muon beamline consisting of curved transport solenoids, only antiprotons of low momentum (say, less than 80 MeV/c) can pass the muon beamline. These antiprotons have very low kinetic energy and velocity. Therefore, they are not suppressed by the beam extinction. There are several ways to suppress antiproton induced backgrounds. They are

- reduction of the production rates of antiprotons by decreasing proton beam energy, and
- absorption in a thin absorber material placed in the muon beamline.

Here, antiproton induced background is sensitive to the incident proton energy. When the incident proton energy is lower, the production of antiprotons are less. The current choice of a proton energy of 8 GeV is chosen so as to reduce the production rate of antiprotons. The first curved section of the muon transport beamline would eliminate antiprotons of high energy. Then, a thin foil of beryllium of 120 μm thickness is placed in the middle section of the beamline to absorb those of low energy.

The production yields of antiprotons for various proton energies are studied by MARS. Also, the energy and angular distributions are modeled based on those of pions. The antiprotons are transported down in the muon beamline in GEANT 3 Monte Carlo simulations. Also based on the MECO experiment [37], expected numbers of electrons and pions in the detector from antiprotons annihilation were studied by using annihilation cross sections experimentally determined. These annihilation products were then tracked with GEANT and the number of particle fluxes coming

to the muon stopping target was calculated. The result shows that primary background resulted from radiative pion capture, and second contribution resulted from electrons scattering in the muon stopping target. Table 6.6 summarizes the results of antiproton induced background [37]. From Table 6.6, the rate of antiproton induced background is about 0.007 at sensitivity of 10^{-16}.

Table 6.6: Antiprotons induced backgrounds for different incident proton momenta.

proton momentum (GeV/c)	number of $\bar{p}/p$ produced	number of $\bar{p}/p$ entering transport	background events
5	3.9×10^{-10}	7.4×10^{-15}	7×10^{-7}
6	5.3×10^{-8}	8.0×10^{-13}	8×10^{-5}
7	1.4×10^{-6}	1.2×10^{-11}	1.2×10^{-3}
8	8.5×10^{-6}	6.8×10^{-11}	7×10^{-3}

6.2.3 Cosmic Ray Induced Background

Cosmic ray-induced electron backgrounds are potentially important background. To reduce this type of backgrounds, active and passive shielding are needed. A passive shielding of 2 meter concrete and 0.5 m of steel might be necessary. Layers of scintillator veto counters surrounding the detector with combined efficiency for charged particle detection of 99.99 % (1 % of inefficiency per layer) are required. In off-line analysis, event selection of eliminating extra particles in the tracking system or in the calorimeter in coincidence with the electron signal might be considered.

The cosmic-ray induced background is estimated by GEANT 3 Monte Carlo simulations. The energy and angular distributions of cosmic rays are determined based on the known parameters. Namely, the energy spectrum at a sea level is essentially flat below 1 GeV, and the flux follows with a power law approximately given by $E^{-2.5}$, with E in GeV. The angular distribution is approximated by $dN/d\theta \sim e^{-1.43\theta}$. The muon flux is about 60 % of positives and 40 % of negatives. Since electrons and muons can be identified by the energy measurement by the calorimeter, electrons from muon decay, δ-ray and pair production become potential backgrounds. By GEANT 3 Monte Carlo simulations, the expected level of cosmic ray-induced backgrounds is less than 0.04 events for one year running of 2×10^7 seconds with a beam duty factor of about 0.2.

6.2.4 Summary of Background Rates

The expected background rates at a sensitivity of 10^{-16} are summarized in Table 6.7.

Table 6.7: Summary of the background rates at a sensitivity of 10^{-16}. Backgrounds identified with an asterisk are proportional to the beam extinction, and the rates in the table assume 10^{-9} beam extinction.

Background	Events	Comments
Muon decay in orbit	0.05	230 keV (sigma) assumed
Pattern recognition errors	<0.001	
Radiative muon capture	<0.001	
Muon capture with neutron emission	<0.001	
Muon capture with charged particle emission	<0.001	
Radiative pion capture*	0.12	prompt pions
Radiative pion capture	0.002	due to late arriving pions
Muon decay in flight*	< 0.02	
Pion decay in flight*	< 0.001	
Beam electrons*	0.08	
Neutron induced*	0.024	for high energy neutrons
Antiproton induced	0.007	for 8 GeV protons
Cosmic rays induced	0.04	with 10^{-4} veto inefficiency
Total	0.34	

Chapter 7

Experimental Layout at J-PARC

7.1 Overview

The experimental setup for $\mu^- - e^-$ conversion will be installed in the J-PARC NP Hall where a slow-extracted proton beam is delivered. The exact location of the muon beamline and the detector is under discussions. The J-PARC NP Hall which is under construction now (winter, 2006), and some of experiment which will be carried out at the NH hall have been officially approved as stage-1 or stage-2. With this being the situation, several constraints have to be taken into account to accommodate the beamline and detector, since showing of our interest in carrying out the experiment is late. Some of them are

- the second target station (in addition to the current T1 target),
- less interference to the other existing experimental areas, and
- proton beam optics.

Additional modifications of infrastructure available in the NP Hall might be needed. With some consultant with the KEK beam-channel group, one of potential layout of the beamline and detector is shown in Fig.7.1 (a 3-dimensional view) and Fig.7.2 (top view). In this layout, a muon beam is taken off upward through the ceiling of the proton beam tunnel so that a hole in the poured concrete shielding is not necessary made. And a potential location shown in the layout will not have any obvious conflicts to experimental areas for the other experiments.

7.2 Second Target Station

In this preliminary layout, the second target station is located downstream from the T1 target. When the second target is in a beam, the T1 target will be up off from a beam. Since a only proton beam power of 7 μA with 8 GeV is needed, the second target station does not necessarily take a full power of the J-PARC beam power of

about 450 kW (15 μA with 30 GeV) [1]. The issues related to the second target station are the following.

- *radiation shielding*
  Shielding for the beam line and target is needed towards top, bottom (floor) and sides (in particular downstream-side). We have calculated that shielding blocks equivalent to about 7 meter thick concrete might be needed. An additional shielding should be placed in the proton beam tunnel and above the ceiling of the tunnel if available. To place additional radiation shielding on the top, a few meter of the beamline concrete blocks from the top might better be cut off. Furthermore, towards the bottom (floor), shielding of heavy material should be placed. Towards downstream, radiation originating from photons should be reduced by copper shielding cooled by water. Detailed calculation of radiation shielding requirements will be done.

- *proton beam optics*
  Proton beam optics to focus a proton beam of 8 GeV to the location of the second target station must be done. Particular care is a proton beam halo. Effects to the superconducting solenoids should be studied. Furthermore, a proton beam has to be defocused at the proton beam dump. Additional optical elements (like quadrapole magnets) should be placed upstream as well as downstream.

[1] It is no doubt that it would be better to have capability of higher beam power.

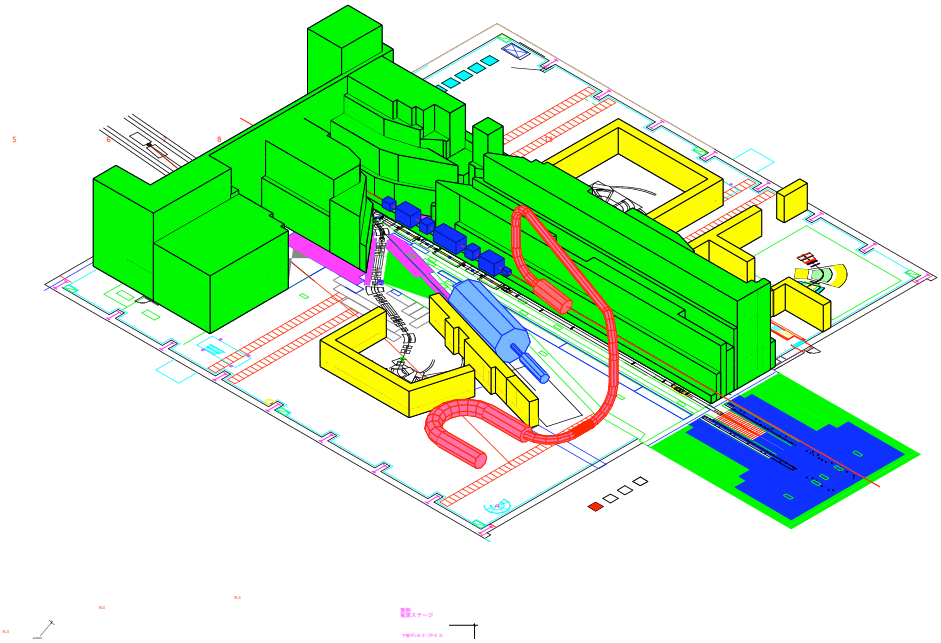

Figure 7.1: A schematic potential layout of the muon beamline and detector shown in pink. (a 3-dimensional view)

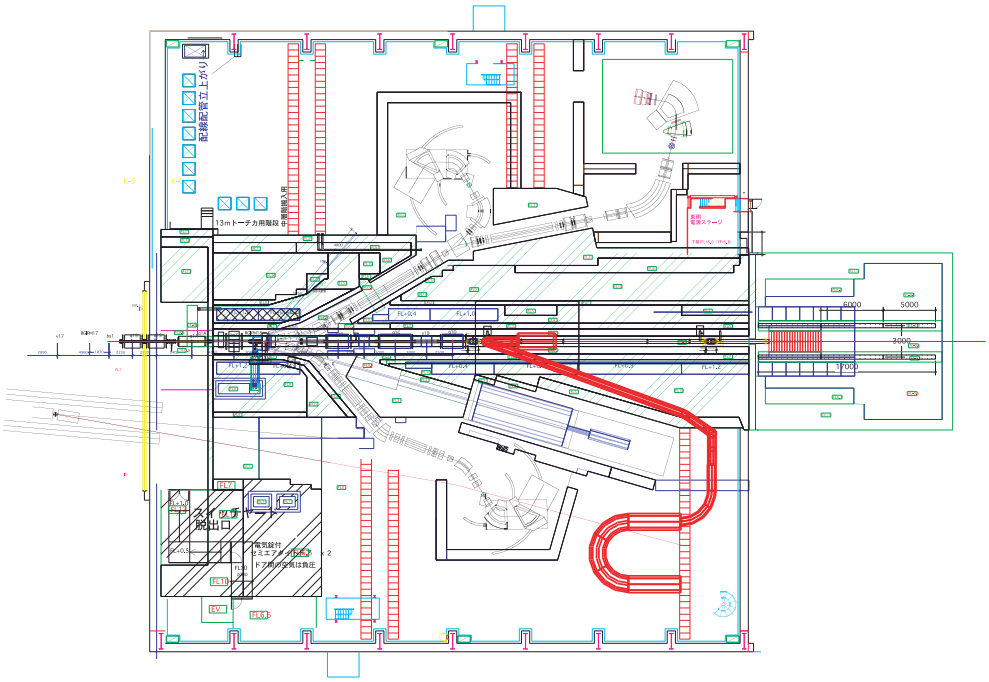

Figure 7.2: A schematic potential layout of the muon beamline and detector shown in pink (a top view)

Chapter 8

Conclusion

We request support to develop a proposal for a new experiment of searching for coherent neutrino-less $\mu^- - e^-$ conversion, $\mu^- + N(A,Z) \rightarrow e^- + N(A,Z)$, at a sensitivity of $B(\mu^- N \rightarrow e^- N) < 10^{-16}$.

The $\mu^- - e^-$ conversion process is one the most promising to seek for lepton flavor violation in the charged lepton systems. The aimed sensitivity is a factor of 10,000 better than that of current experiments. This experiment would offer powerful probe for new physics phenomena beyond the Standard Model, such as supersymmetric grand unification models and supersymmetric seesaw models with heavy right-handed Majorana neutrinos.

To search for $\mu^- - e^-$ conversion process in an aluminum target, where a single electron of the energy of 105 MeV is detected, a new muon beam with high intensity and high quality is needed. The muon beam line that considered and designed consists of high-field pion capture solenoids, curved solenoids to select beam momenta, and a curved solenoid spectrometer to detect $\mu^- - e^-$ conversion with low-counting-rate conditions. The experiment is planned to be carried out in the J-PARC NP Hall by using a bunched proton beam slowly extracted from the J-PARC main ring, where beam bunching is needed to eliminate beam-related backgrounds.

This new initiative has been taken to achieve an early and timely start of a series of searches and is regarded as the first step of our staging approach continuing toward the ultimate search and the discovery of $\mu^- - e^-$ conversion.

Bibliography

[1] Kuno Y and Okada Y, 2001 *Rev. of Mod. Phys.* **73** 151

[2] Hincks E P and Pontecorvo B 1947 *Phys. Rev. Lett.* **73** 246

[3] Brooks M L *et al.* (MEGA Collaboration) 1999 *Phys. Rev. Lett.* **83** 1521

[4] Bellgardt U *et al.* 1988 *Nucl. Phys.* B **229** 1

[5] Wintz P 1998 in *Proceedings of the First International Symposium on Lepton and Baryon Number Violation*, edited by H.V. Klapdor-Kleingrothaus and I.V. Krivosheina (Institute of Physics Publishing, Bristol and Philadelphia), p.534. Unpublished.

[6] Willmann L *et al.* 1999 *Phys. Rev. Lett.* **82** 49

[7] K. Hayasaka *et al.* (Belle Collaboration) 2005 *Phys. Lett.* B **613** 20

[8] K. Abe *et al.* (Belle Collaboration) 2004 *Phys. Rev. Lett.* **92** 171802

[9] B. Aubert *et al.* (BaBar Collaboration) 2004 *Phys. Rev. Lett.* **92** 121801

[10] Krolak P *et al.* 1994 *Phys. Lett.* B **320** 407

[11] Ambrose D *et al.* (BNL E871 Collaboration) 1998 *Phys. Rev. Lett.* **81** 5734

[12] Lee A M *et al.* 1990 *Phys. Rev. Lett.* **64** 165

[13] Arisaka K *et al.* 1998 *Phys. Lett.* B **432** 230

[14] Akers R *et al.* (OPAL Collaboration) 1995 *Z. Phys.* C **67** 555

[15] Abreu P *et al.* (DELPHI Collaboration) 1997 *Z. Phys.* C **73** 243

[16] Hall L J, Kostelecky V A and Raby S 1986 *Nuclear Physics* B **267** 415

[17] Barbieri R, Hall L and Strumia A 1995 *Nuclear Physics* B **445** 219

[18] Hisano J, Moroi T, Tobe K, and Yamaguchi M 1997 *Phys. Lett.* B **391** 341; Erratum 1997 *Physics Letters* B **397** 357

[19] Hisano J, Moroi T, Tobe T, Yamaguchi M, and Yanagida T 1995 *Phys. Lett.* B **357** 576

[20] Hisano J, Nomura D, and Yanagida T 1998 *Physics Letters* B **437** 351

[21] Hisano J and Nomura D 1999 *Phys. Rev.* D **59** 116005

[22] Kosmas T S, Faessler A and Vergados J D 1997 *J. Phys. G* **23** 693; Kosmas T S and Vargados J D 1996 *Phys. Rep.* **264** 251; Shanker O 1979 *Physics Review* D **20** 1608

[23] Czarnechi A, Marciano W J and Melnikov K 1998 *Coherent Muon-Electron Conversion in Muonic Atoms* Preprint BNL-HET-98/2, TTP 97-19, hep-ph/9801218

[24] Raidal M and Santamaria A 1998 *Phys. Lett.* B **421** 250

[25] Bryman D A, Blecher M, Gotow K and Powers R J 1972 *Phys. Rev. Lett.* **28** 1469

[26] Badertscher A *et al.* 1982 *Nucl. Phys.* A **377** 406

[27] Bryman D A *et al.* 1985 *Phys. Rev. Lett.* **55** 465

[28] Ahmad S *et al.* 1988 *Phys. Rev.* D **38** 2102

[29] Dohmen C *et al.* (SINDRUM II Collaboration) 1993 *Phys. Lett.* B **317** 631

[30] Honecker W *et al.* (SINDRUM II Collaboration) 1996 *Phys. Rev. Lett.* **76** 200

[31] Bachman M *et al.* 1997, a research proposal to Brookhaven National Laboratory AGS "A Search for $\mu^- N \to e^- N$ with Sensitivity Below 10^{-16}, **M**uon – **E**lectron **CO**nversion"

[32] Dzhilkibaev R M and Lobashev V M 1989 *Sov. J. Nucl. Phys.* **49** 384

[33] Barkov L M *et al.* 1999, a research proposal to PSI "Search for $\mu^+ \to e^+\gamma$ down to 10^{-14} branching ratio"

[34] A Letter of Intent to the J-PARC 50 GeV Proton Synchrotron Experiments, "The PRISM Project - A Muon Source o the World-Highest Brightness by Phase Rotation -", January 1st, 2003

[35] A Letter of Intent to the J-PARC 50 GeV Proton Synchrotron Experiments, "An Experimental Search for the $\mu^- - e^-$ Conversion Process At An Ultimate Sensitivity Of The Order of 10^{-18} With PRISM", January 1st, 2003

[36] A Letter of Intent to the J-PARC 50 GeV Proton Synchrotron Experiments, "An Experimental Search for a $\mu^- - e^-$ Conversion at Sensitivity of the Order of 10^{-18} With A Highly Intense Muon Source, PRISM". April 28th, 2006.

[37] MECO Technical Proposal, August 1, 2001, unpublished.

[38] MECO Superconducting Solenoid System Conceptual Design Report, June 6, 2002, unpublished.

[39] *http://g4beamline.muonsinc.com*

[40] Hänggi P, Viollier R D, Raff U nd Adler K 1974 *Phys. Lett.* B **51** 119

[41] Herzog F and Adler K 1980 *Helv. Phys. Acta* **53** 53

[42] Shanker O 1982 *Phys. Rev.* D **25** 1847

[43] R. Watanabe, M. Fukui, H. Ohtsubo and M. Morita, 1987 *Prog. Theor. Phys.* **78** 114; R. Watanabe, K. Muto, T. Oda, T. Niwa, H. Ohtsubo, R. Morita and M. Morita, 1993 *At. Data Nucl. Data Tables* **54** 165

[44] T. Kozlowski *et al.*, 1985 *Nucl. Phys.* A **436** 717

[45] A. Wyttenbach *et al.*, 1978 *Nucl. Phys.* A **294** 278

[46] K. S. Krane *et al.*, 1979 *Phys. Rev.* C **20** 1873

Appendix A

PRISM FFAG Ring Development

A.1 Overview

One of advantages of this new initiative is its upgradability. The current design of this experiment well fits the original design of $\mu^- - e^-$ conversion experiment with PRISM (Phase Rotated Intense Slow Muon).

Fig. A.1 shows the schematic layout of PRISM and its detector PRIME. The difference between the PRISM/PRIME and this initiative is the existence of "Muon Phase Rotation Section". Thus, it is relatively easy to upgrade the current initiative to the full-set of PRISM; by introducing the Muon Phase Rotation Section, and the ultimate sensitivity of 10^{-18}, which is two orders of magnitudes higher than the current initiative, will become achievable.

By introducing the Muon Phase Rotation Section, the muon beam will become:

- higher in purity,
- narrower in energy width.

The beam related background will be further reduce by the former improvement, and the muon decay-in-orbit background will be reduced by the latter improvement.

The currently on-going activities for the realization of the Muon Phase Rotation Section are in three fields:

- PRISM-FFAG magnet development,
- High field RF development,
- Fast kicker system development.

A.2 PRISM-FFAG Magnet Development

The required parameters for the PRISM-FFAG ring are summarized in Table A.1. We adopted a scaled-radial-sector-type FFAG (fixed field alternating gradient) synchrotron with triplet focusing.

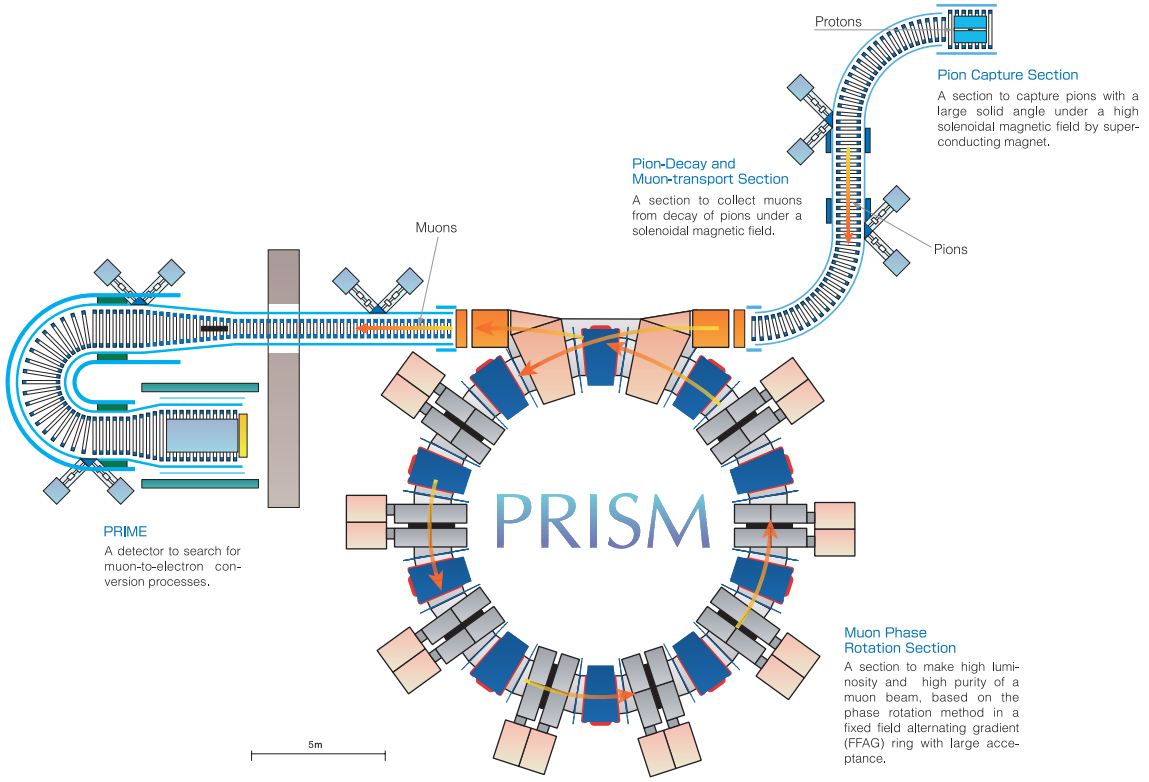

Figure A.1: Schematic layout of full PRISM and PRIME detector.

A cross sectional view of the PRISM-FFAG magnet on a median plane is shown in Fig. A.2. The magnet is a scaled-radial-sector magnet with triplet focusing and consist of three poles (DFD), and a pair of field clamp; the field clamps are equipped so as to reduce a leakage of magnetic flux into RF cores which are located between the two magnet cells. The F and D poles are magnetically short-circuited by common iron top poles. This configuration make reduction of a magnetic flux density in return yoke, compared to the magnets whose F and D poles are separated off. As the result, a total yoke weight can be reduced, and in fact, it can be reduced by 30%, compared to the separated magnets.

In the scaled-radial-sector-FFAG synchrotron, the distribution of an FFAG magnetic field is given by

$$B(r) = B_0(r/r_0)^k, \tag{A.1}$$

Parameter	value
Momentum acceptance	68 MeV/c $\pm$20 %
Transverse acceptance	38,000 πmm·mrad $\times$ 6,000 πmm·mrad
Equilibrium radius	6.5m @ 68 MeV/c

Table A.1: Parameters for the PRISM-FFAG ring

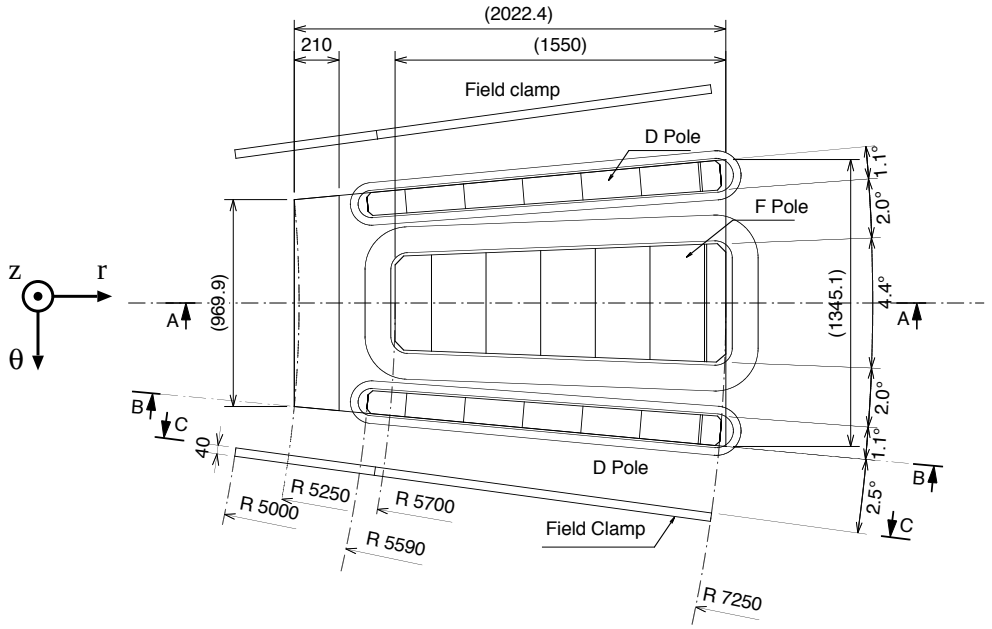

Figure A.2: The cross sectional view of the PRISM-FFAG magnet on a median plane.

where r is the distance from a center of the FFAG ring and k is a field index and constant for the machine [1]. To generate the field gradient, the gap heights of magnet poles are varied as a function of radial position. The aperture size of the magnet is more than 0.3 m in vertical at outer side and $\sim$1 m in horizontal. The effective-vertical aperture, where a thickness of a vacuum beam duct is considered, is about 10 times larger than the proton FFAG magnet developed at KEK [2].

The magnet design parameters which are required from a beam optics study [3] are shown in Table A.2. The pole shape and magnetomotive force have been adjusted by iteratively calculating a 3-D magnetic field with help of a 3-D field analysis code, TOSCA (Vector Fields LTD [4]) so as to meet the parameters.

Fig. A.3 shows a calculated- and a measured azimuthal filed distribution at the

Parameters	values
Number of cells	10
Field index (k)	4.6
Aperture	0.3 m $\times$ 1.0 m
Equilibrium radius	6.5m
$B_F L$ at $r = 6.5$ m	0.0855 T·m/half cell
$B_D L$ at $r = 6.5$ m	0.0143 T·m/half cell
F/D ratio	6
Opening angle of F pole	4.4 degree
Opening angle of D pole	1.1 degree

Table A.2: Main parameters of PRISM-FFAG magnet

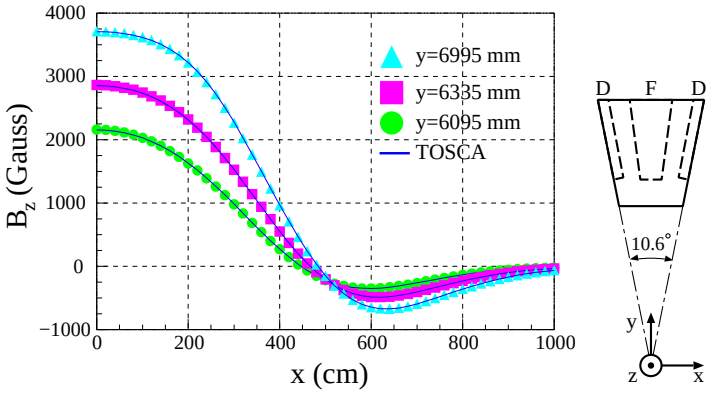

Figure A.3: Azimuthal field distribution of PRISM-FFAG magnet at the median plane. Symboles for the filed-measurement result, and lines for the TOSCA calculation. A coordinate definition in the plot is shown the right of the plot.

median plane.

A.2.1 Ring Acceptance

Particle tracking simulations have been performed by using GEANT 3 [5] in order to estimate the ring acceptance with this magnet. Fig. A.4 shows betatron tunes plotted as a function of the muon momenta. It is found that the horizontal and vertical tunes does not vary over the momentum range from 54.4 MeV/c to 81.6 MeV/c.

Fig. A.5 shows a simulated 4D acceptnace(r, r', z, z') as a function of the muon momentum. The 4D acceptance of 6.0×10^8 mm^2·mrad^2 has been achieved at 68 MeV/c, and the momentum acceptance is about $\pm$ 20%.

A.3 RF System Development

In order to complete the quick phase rotation before muons decay away in 2.2 μsec, RF system has to provide quite high field gradient. The RF parameters are listed in Table A.3.

RF frequency	5MHz
Total RF voltage	2-3 MV
Field gradient of RF	$\geq$ 0.2 MV/m
Cavity length	0.33 m
Size of Beam Pipe	1 m (H) $\times$ 0.3 m(V)
Gap voltage	66 kV
Duty factor	0.1 % (100 Hz $\times$ 10 μ s)

Table A.3: PRISM RF Parameters.

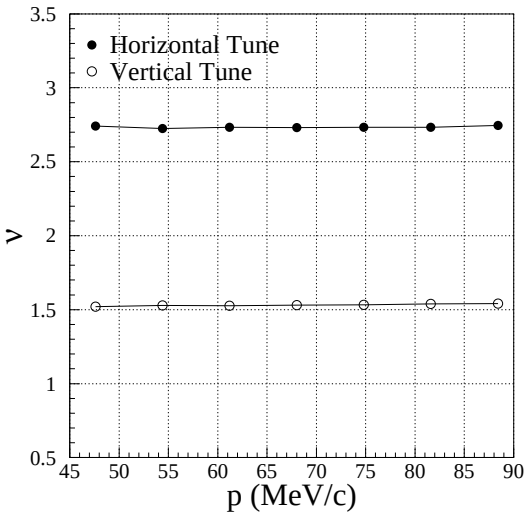

Figure A.4: Betatron tune as a function of muon momenta. Closed circles: Horizontal tune. Open circles: Vertical tune.

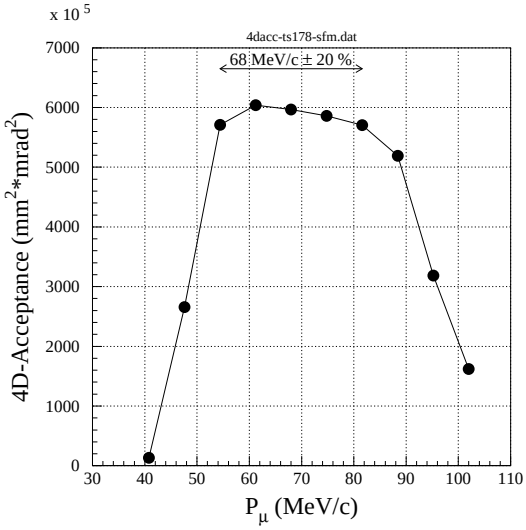

Figure A.5: 4D transverse acceptance as a function of muon momenta.

There are three key issues to realize the system as follows,

- Low duty factor,
- High gap voltage,
- Short cavity length.

We adopted a magnetic alloy (MA) core, which is widely used in many hadron accelerators [6]. The shunt impedance of PRISM MA core is about 150 Ω, and 6 cores will be installed in a cavity. Figure A.6 shows the photograph of the MA core for the PRISM RF. The size of the core is 1.7 m (H) × 1 m (V) × 35mm(T).

To obtain high gap voltage, the tube anode voltage was set at the maximum voltage for tube operation. We developed the DC blocking capacitors which can stand for 40 kV(DC) and +33 kV(RF) as well as feed-through type ones which can stand for 40 kV(DC).

Figure A.7 shows result of the bench test of the prototype of the high power amplifier. The gap voltage of 43 kV was achived, and this corresponds to the requirement on the driving RF current for PRISM.

A.4 Kicker System Development

Muons from the decay solenoid section are injected into the PRISM-FFAG ring in order to reduce the momentum spread. The injected muon beam has a large radial beam size (∼1 m in horizontal and ∼0.3 m in vertical) due to its ±20% momentum spread, where the time distribution (longitudinal bunch length) is 40 nsec with a 240

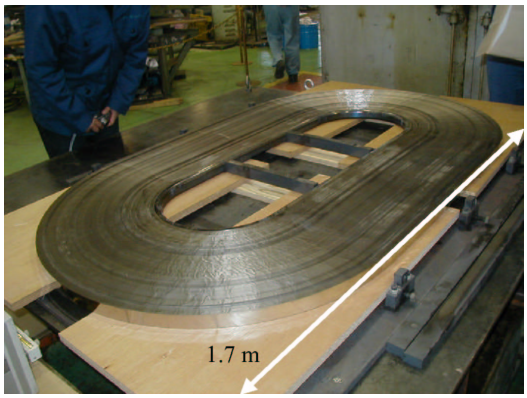

Figure A.6: Magnetic alloy core of PRISM-FFAG.

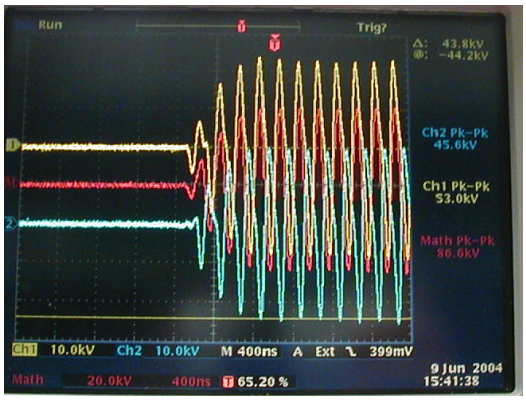

Figure A.7: Measured gap voltage.

nsec bunch gap. Since injection/extraction kicker magnets are installed in the straight section of the PRISM-FFAG ring, large aperture of kicker magnets are required.

While the momentum spread is reduced to be $\pm 2\%$ after the phase rotation in the PRISM-FFAG ring, the bunch length is expanded and the bunch gap becomes as shorter as only 80 nsec. In order to extract such a short-gap bunched-beam, the kicker magnetic field should be rise within the bunch gap.

The requriement to the PRISM-FFAG ring kicker system is as follows:

- large aperture: $\sim$1 m in horizontal and $\sim$0.3 m in vertical,
- short length: 0.5$\sim$1.5 m since the length of straight section is very limited,
- fast rise time: < 80 nsec.

In order to fulfill the requirements while retaining the operation being robust and reliable, we proposed a new scheme; a lumped type magnet with All Pass Network (APN) as shown in Fig. A.8. The input impedance of APN is principally equal to the termination resistance in any frequency range, and so we can treat the kicker magnet as just lumped type one.

Comparing with a conventional scheme; transmission line type kicker that is needed to be enclosed in a vacuum vessel, there is no great difference in rise time characteristic and power consumption. However, the constant impedance characteristic and the simple structure without any electrode are great advantage. This is very helpful for the installation of the kicker magnet into the limited straight section.

The new scheme is compared with conventional one using SPICE simulation as shown in Fig. A.9. The current rise time in the new scheme is a little bit faster, but it is not so different. Although the input impedance of the conventional scheme depends on frequency above a cutoff frequency, such dependence cannot be seen in the new scheme. The full range impedance matching is expected.

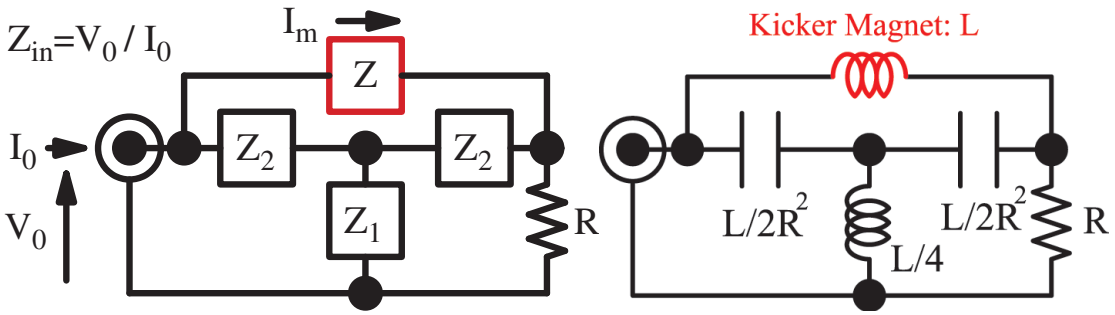

Figure A.8: All Pass Network (left) and lumped type kicker magnet with APN (right). The input impedance z is principally equal to the termination resistance R in the case of $z_1 + z_2/2 = R^2[1/z + 1/(2z_2)]$.

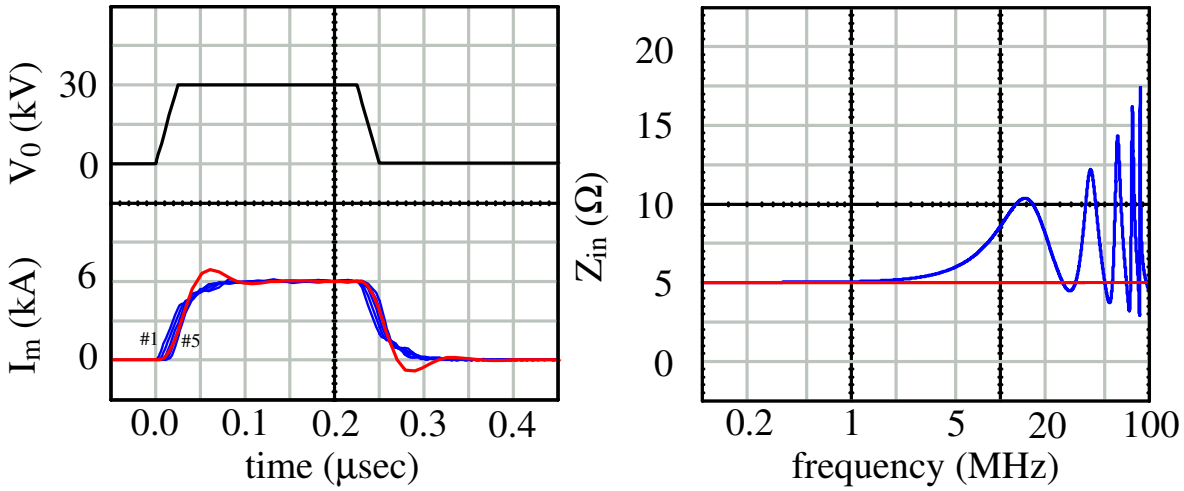

Figure A.9: Comparison between schemes calculated by SPICE simulation. Red and blue lines respectively show the results of new and conventional schemes on the pulse responses (left) and the input impedances (right).

Bibliography

[1] K. R. Symon and D. W. Kerst and L. W. Jones and L. J. Laslett and K. M. Terwilliger, 1956 *Phys. Rev.* **103** 1837

[2] T. Adachi, *et. al.* 2001 in *Proceedings of PAC 2001* 3254

[3] A. Sato, *et. al.* 2004 in *Proceedings of The 17th International Conference on Cyclotrons and Their Applications, Cyclotrons 2004* 235

[4] Vector Fields LTD, web site: http://www.vectorfields.com/

[5] Application Software Group Computing and Networks Division, *GEANT, Detector Description and Simulation Tool*, CERN (1994)

[6] C. Ohmori, *et. al.* 2004 in *Proceeding of EPAC2004* 123